JOURNAL OF GEOPHYSICAL RESEARCH, VOL. 97, NO. C6, PAGES 9565–9593, JUNE 15, 1992

The Barotropic Electromagnetic and Pressure Experiment 1. Barotropic Current Response to Atmospheric Forcing

ALAN D. CHAVE[1]

AT&T Bell Laboratories, Murray Hill, New Jersey

DOUGLAS S. LUTHER AND JEAN H. FILLOUX

Scripps Institution of Oceanography, La Jolla, California

During 1986–1987, an array of horizontal electrometers (which measure the subinertial barotropic velocity) was deployed for 11 months in the central North Pacific to study atmospherically forced motions in a low eddy kinetic energy region. Significant coherence is found to be ubiquitous between the barotropic velocity and one or more surface atmospheric variables over the North Pacific. The maximum squared coherence between currents and wind stress curl at all periods greater than 3 days is typically 0.6, rarely below 0.4, and occasionally above 0.8, and is dominantly nonlocal, although local coherence is seen at some sites, especially at the shorter periods. Both the coherence and the intersite pattern similarity are strongest at the periods of relative maxima in the barotropic current autospectra (e.g., at 6–8, 10–14, and 20–50 days). The locations at which the wind stress curl forces the motions at each site and for each period have been determined. While there is substantial intersite variability, some of the observed patterns of squared coherence over the North Pacific are very similar to those predicted by simple, linear, smooth-bottomed, quasi-geostrophic models of atmospherically forced barotropic currents. The forcing location is occasionally found to be the same spot for all oceanic instruments, especially at the autospectral maxima in barotropic current. More commonly, distinct forcing locations are found for each instrument even when closely spaced, suggesting topographic influence. In other cases, multiple forcing locations are implicated for the motions at a single station. All of this site- and period-dependent variability of the forcing location is incompatible with the simple models and is due either to the known spatial inhomogeneity of the curl forcing field or to topographic effects. The importance of the former is emphasized using simple arguments based on analytic transfer functions between the atmospheric and oceanic variables and on observed wavenumber spectra for wind stress curl. Quantitative assessment of topographic effects must await suitable numerical models. In addition, maximum likelihood wavenumber spectra of the barotropic currents have been estimated in those bands with an adequate number of coherent sensors. The wavenumbers at the spectral peaks are compatible with the dispersion relation for Rossby waves modified by the observed, large-scale, linearly sloping topography which shoals to the northeast. The observed group velocities are in general quite consistent with the inferred forcing locations based on the ocean-atmosphere coherences.

1. INTRODUCTION

Except in the vicinity of unstable boundary currents, most of the barotropic fluctuations observed in the deep ocean at periods of days to months are apparently directly, atmospherically forced. Observational evidence for both local and nonlocal coherence between ocean currents or seafloor pressure and the wind forcing in areas of weak to moderate eddy variability is rapidly accumulating [e.g., *Dickson et al.*, 1982; *Koblinsky and Niiler*, 1982; *Niiler and Koblinsky*, 1985; *Brink*, 1989; *Luther et al.*, 1990; *Samelson*, 1990; *Cummins and Freeland*, 1992]. These data are at least partially explained by a series of model studies based on linear, viscid, quasi-geostrophic dynamics with prescribed atmospheric forcing [e.g., *Frankignoul and Müller*, 1979; *Willebrand et al.*, 1980; *Müller and Frankignoul*, 1981; *Brink*, 1989; *Samelson*, 1989; *Samelson and Shrayer*, 1991; *Cummins*, 1991]. While the successes are encouraging, further model refinement supported by more focussed observational programs is essential to gaining a more complete understanding of atmospherically forced variability.

This paper describes an extensive array of barotropic current measurements collected during the Barotropic Electromagnetic and Pressure Experiment (BEMPEX) in 1986–1987 and examines their relation to atmospheric forcing in detail. In a second paper (D.S. Luther et al., The Barotropic Electromagnetic and Pressure Experiment, 2, Pressure field response to atmospheric forcing, submitted to *Journal of Geophysical Research*, 1992, hereinafter designated Luther et al., 1992), evidence is presented for atmospheric forcing in a complementary array of seafloor pressure data from the same experiment. The primary oceanographic objectives of BEMPEX are described by *Luther et al.* [1987] and emphasize studies of atmospheric forcing phenomenology, including quantitative descriptions of the relationships of the pressure and barotropic current fields to the atmospheric variables in frequency space and estimates of the frequency-wavenumber characteristics of any oceanic disturbances which may ensue. Some preliminary results have been reported by *Luther et al.* [1990].

The remainder of this paper is organized into six sections. Section 2 reviews the physics of atmospherically forced oceanic motions, examines pertinent results from previous model studies and field experiments, and summarizes some real properties of

[1]Now at Woods Hole Oceanographic Institution, Woods Hole, Massachusetts.

Copyright 1992 by the American Geophysical Union.

Paper number 92JC00549.
0148-0227/92/92JC-00549$05.00

the wind stress curl field. Section 3 describes the BEMPEX array and instrumentation, with the emphasis on horizontal electric field measurements of the depth-averaged or barotropic velocity at a point. Section 4 considers the barotropic current data in frequency space, noting the common presence of weak spectral enhancements in the 20-to-50-day, 10-to-14-day, and 6-to-8-day bands. Section 5 examines the spatial relations between the barotropic currents and the atmospheric variables by constructing coherence maps for 7 barotropic current sensors in 15 overlapping frequency bands covering the 3-to-300 day range, demonstrating that coherence with the atmosphere is ubiquitous, but considerable intersite variability of the coherence pattern is common. While there are some similarities to model predictions for some bands at some sites, the number of discrepancies is quite large. Common spatial patterns at different stations are observed primarily in those frequency bands where the barotropic velocity exhibits enhanced power. Section 6 presents maximum likelihood wavenumber spectra for the barotropic velocity field constructed using coherent subarrays of the available instruments. The wavenumber spectra are used to demonstrate consistency of the data with simple, linear Rossby wave dynamics in the presence of the large scale, linearly sloping topography observed in the study area. However, westward group velocity is inferred dominantly in the zonal velocity component at periods longer than 10 days, while eastward group velocities are required at shorter periods for the meridional component. Section 7 attempts to reconcile the coherence and wavenumber results with simple theories, makes some comparisons with published model results, and contains suggestions for further work.

2. ATMOSPHERICALLY FORCED OCEANIC VARIABILITY

In a classic review, *Philander* [1978] gave a comprehensive look at the linear response of an ocean to forcing at a specified frequency and wavenumber. Under the β plane approximation, he showed that the vertical velocity w at the base of a mixed layer of thickness D is given by

$$\mathbf{L}(w) = -f\,\hat{z}\cdot\nabla\times\vec{\tau} - \beta\tau_x - \partial_t\nabla\cdot\vec{\tau} + D\beta\partial_x P_s + D\nabla^2\partial_t P_s \quad (1)$$

where $\mathbf{L}$ is a complicated differential operator, $\vec{\tau}$ is the wind stress which acts as a body force in the mixed layer, and P_s is the atmospheric pressure which is imposed at the sea surface. For forcing with an intrinsic angular frequency ω and horizontal length scale L, the five components of the right hand side of (1) are in the ratio $1 : \beta L/f : \omega/f : D\beta|P_s|/f|\tau| : \omega D|P_s|/fL|\tau|$. At the center of the BEMPEX array (40°N, 163°W), the standard deviations of the wind stress and air pressure computed from the Fleet Numerical Oceanography Center (FNOC) product are 3 dyn cm^{-2} and 13 mbar or 3000 dyn cm^{-2}, respectively. These values are dominated by the most energetic disturbances in the 2-to-5-day band, but since their ratio is of immediate interest and spectra of the wind stress and air pressure have similar forms, the frequency dependence will be neglected. Choosing a mixed layer depth of 50 m and confining consideration to long-period (>4 days), large scale (>500 km) disturbances allows the relative importance of the five terms to be evaluated. The third, wind stress divergence term is only one fifth of the wind stress curl term at 4-days period and is increasingly insignificant at longer periods independent of the forcing scale. The fourth, zonal air pressure gradient term is about a hundredth of the wind stress curl term independent of the length and time scales. The fifth, air pressure Laplacian term decreases in relative importance with both period and length scale and is only a fiftieth the size of the wind stress curl term at a period of 4 days when L=500 km. Consequently, air pressure forcing will have negligible importance. The second term is also small compared with the first except when the length scale is larger than several thousand kilometers. Thus, the dominant atmospheric forcing mechanism is represented by the vertical component of the wind stress curl (hereinafter simply curl), and other forcing terms will be neglected for the remainder of this paper. However, establishing that the dominant atmospheric driving term is proportional to curl does not preclude strong coherence of an oceanic velocity or pressure measurement with either wind stress or surface air pressure. This is because the wind stress and air pressure are themselves coherent with curl and hence can serve as proxies. Since either air pressure or wind stress are expected to contain less noise than curl, it might be expected that stronger coherence of an oceanic variable will be observed with the first two quantities.

While the importance of curl as the dominant forcing function is established, this does not by itself prove that atmospherically induced oceanic variability will be larger than that due to other driving mechanisms. The decades-long debate on the degree to which subinertial fluctuations in the deep ocean are directly wind driven has recently yielded a number of theoretical models that predict energy levels and coherences between oceanic and atmospheric variables at points distant from energetic boundary currents with some success and suggest that atmospheric forcing is energetically important [*Frankignoul and Müller*, 1979; *Willebrand et al.*, 1980; *Müller and Frankignoul*, 1981; *Brink*, 1989; *Samelson*, 1989; *Samelson and Shrayer*, 1991; *Cummins*, 1991; *Cummins and Freeland*, 1992]. All of the models are based on linear, viscid, quasi-geostrophic dynamics with prescribed wind forcing and generally consider only constant depth or, at most, linearly sloping seafloor geometries with either unbounded or bounded edge conditions.

For a flat-bottomed basin, the character of the oceanic response can be divided into several regimes according to the matchup of the forcing and the oceanic response in frequency-wavenumber space. At periods shorter than the Rossby wave cutoff where no free waves can exist, the only possible response is an evanescent one. Except for relatively unenergetic, short horizontal scales of the forcing or for periods close to the inertial, the vertical decay scale is much larger than the water depth and hence the motion is effectively barotropic. Significant local coherences between specific oceanic and atmospheric variables (i.e., bottom pressure and air pressure, zonal velocity and zonal wind stress, meridional velocity and meridional wind stress, and bottom pressure and curl) as well as significant horizontal coherences between the oceanic variables are expected in this range. At somewhat longer periods, freely propagating barotropic Rossby waves can exist while the baroclinic response remains evanescent. The extent of the local coherence depends critically on the wavenumber bandwidth of the free Rossby waves, and in particular on the amount of friction as a function of horizontal scale. In general, the local coherence is expected to drop compared with that at shorter periods. However, this does not preclude significant nonlocal coherence of the oceanic and atmospheric variables as the Rossby waves serve to transport information in the form of coherence along the direction of their group velocity, a fact which was first recognized by *Brink* [1989]. The maximum nonlocal coherence is expected to occur most often to the east because long Rossby waves are damped less than their short-scale counterparts, but western coherence is not excluded, especially at periods approaching the cutoff.

At even longer periods (>100 days), the large-scale Rossby

waves which carry energy westward, including free baroclinic waves, have weak relative vorticity, and the short-scale eastward waves are more heavily damped. Since the forcing is also weaker at short scales, this leaves an approximate Sverdrup balance where meridional currents are strongly coherent with local curl. However, the existence of a Sverdrup balance may easily be altered by topography in the real ocean, hence should not be regarded as a robust diagnostic feature.

Topography can change this simple scenario through the generation of vorticity on a variety of scales. *Rhines* [1970] showed that the vertical structure of Rossby waves is altered by bottom topography, but this effect is restricted to frequencies close to those of free, flat-bottom baroclinic waves and hence is unimportant at periods under ≈100 days. However, water movement across isobaths results in a new restoring force that alters the frequencies and wavenumbers of free barotropic Rossby waves. For instance, from conservation of potential vorticity, the effect of linearly sloping topography can be understood as a change in the magnitude of the potential vorticity gradient with coordinate system rotation according to the direction of the slope [*Rhines*, 1969]. *Koblinsky* [1990] has examined the global distribution of the planetary component of potential vorticity f/H (hereinafter, simply planetary vorticity) using real topography smoothed over a ≈200-km scale, showing that for the mid-latitude North Pacific the slopes tend to enhance the potential vorticity gradient so that effective beta ($\beta_e \equiv |\nabla(f/H)|$) increases over that for a flat-bottomed ocean. In such a regime, the oceanic barotropic response will be dominated by nonlocal forcing since the evanescent response band is shifted to shorter periods. However, small regions where topography results in weak β_e are scattered throughout the mid-latitude ocean, so that the free Rossby wave band is shifted to long periods and the only possible response is local and evanescent. The overall effect of topography is a shifting and blurring of the transition periods between the three dynamical regimes described earlier, and possibly the complete absence of some of them.

The earliest of the models which had some success in predicting wind-forced deep ocean fluctuations were based either on a numerical approach driven by real winds [*Willebrand et al.*, 1980] or on a stochastic methodology and an analytic specification for curl [*Frankignoul and Müller*, 1979; *Müller and Frankignoul*, 1981]. All of these studies considered only the local coherence between a given oceanic variable and atmospheric fluctuations immediately above it. Their predictions yielded the three dynamic regimes outlined earlier, with strong local coherence in the short period, evanescent range, negligible local coherence in the free wave range, and local coherence (due to an approximate Sverdrup balance) at periods longer than ≈100 days. Model predictions for eddy kinetic energy and subsurface displacement were in rough agreement with existing measurements, but meager applicable data precluded extensive coherence comparisons. Nevertheless, these studies concluded that the atmosphere could be the most important source of eddy variability in weak mean flow regions. In addition, the stochastic model of *Müller and Frankignoul* [1981] provides simple analytic expressions for the atmospheric-to-oceanic transfer functions which give considerable insight into the physics of atmospherically forced motions in frequency-wavenumber space, and could easily be extended to study nonlocal coherence.

Perhaps the earliest clear inference of atmospheric forcing in regions of weak mean flow was given by *Dickson et al.* [1982], who found a strong seasonal dependence to deep eddy kinetic energy in the 3-to-80-day band in the eastern North Atlantic which peaked during winter. Direct observations of a local Sverdrup balance are presented by *Koblinsky and Niiler* [1982] for the subtropical North Atlantic and by *Niiler and Koblinsky* [1985] for the North Pacific. The latter study showed a Sverdrup balance at surprisingly short periods (≈10 days) with nearly barotropic currents. This indicates a lack of short scale Rossby waves compared with the model predictions of both *Willebrand et al.* [1980] and *Müller and Frankignoul* [1981], possibly due to an excess of curl energy over the real ocean at scales larger than 500 km or to underdamping of short-scale waves in the models. However, a subsequent examination of 200 instrument years of North Pacific current meter data by *Koblinsky et al.* [1989] found only occasional local coherence between currents and curl, indicating that a Sverdrup balance is not common. Nevertheless, Koblinsky et al. suggested that topographic Sverdrup dynamics accounted for the observed seasonal modulation of abyssal eddy kinetic energy in the 10-to-100-day band. Subsequently, *Cummins* [1991] used a stochastically forced numerical model that incorporated real topography to conclude that the dominant vorticity balance at a point is wavelike at periods below 100 days for the subpolar North Pacific, refuting Koblinsky et al.'s contention. A topographic Sverdrup balance emerges only when relatively large scale (several degrees) areal averages of the vorticity equation terms are taken, implying that point measurements are influenced by topographically generated small-scale velocity components.

Brink [1989] presented a theoretical framework for the wind-driven flow that emphasized the importance of distant forcing points. Significantly, he recognized that Rossby waves excited by curl can transport information in the form of coherence between the oceanic and atmospheric variables along the direction of group propagation. The model Brink proposed was a semi-analytic, quasi-geostrophic type with a simple, unimodal spatial autocorrelation function for curl whose energy level was independent of latitude. Not surprisingly, results indicated different ocean-atmosphere coherences for the zonal and meridional velocities. The coherence pattern for the zonal velocity with curl is nonlocal and displaced to the east, having the form of double-lobes arranged symmetrically north and south of the ocean observer's latitude. For the meridional velocity, a local coherence with curl (Sverdrup balance) obtains. The peak squared coherence was about 0.2, although this depends critically on the friction parameterization and on the curl structure. While Brink found some agreement of the model predictions with the coherence between a single, shallow current meter in the western North Atlantic and curl computed from the FNOC wind product, the model eddy kinetic energy level was two decades below that of the data.

Subsequently, *Samelson* [1989] added vertical shear, a uniform meridional bottom slope, and a deep meridional wall to represent the Mid-Atlantic Ridge in an attempt to reconcile Brink's observations, with only partial success. However, *Samelson* [1990] showed that the coherence between deep currents in the eastern North Atlantic and curl, as well as the eddy kinetic energy levels, were in reasonable agreement with the model, suggesting the presence of a strong non-atmospherically forced component in Brink's western North Atlantic data.

Both Brink's and Samelson's studies predict the existence of weak shifts of the coherence pattern with period. At long periods (49 days), the twin zonal current coherence peaks are displaced about 1500 km to the east of the observer (depending on curl wavenumber bandwidth), while at short periods (5 days)

they are located symmetrically north and south. The meridional current coherence pattern also shows such shifts, with the coherent patch located to the east and west of the observation point at long and short periods, respectively. *Samelson and Shrayer* [1991] further modified the earlier Samelson models to allow for a northward increase in curl power, finding that a northward bias in the coherence patterns results. In particular, the southern lobe of the zonal current double-lobe pattern vanishes, while the meridional current coherent patch is displaced slightly to the north.

While they have given considerable insight into the physics of wind-forced flow, it is likely that the semi-analytic approaches taken in most of the cited studies have been extended to their logical limit. For example, it is not possible to include realistic topography without using a numerical approach, and it is probable that topography exerts a strong influence when the relevant oceanic wavelengths are less than basin scale. Another shortcoming of the models is the oversimplification of curl behavior. *Chave et al.* [1991] have examined the frequency-wavenumber variations of curl in the eastern North Pacific for a 3-year interval, finding considerable variability in the wavenumber spectrum over time scales of a few months and consistent east-west and north-south asymmetries of the spectra at periods under ≈10 days for mid-latitudes. In particular, the observed wavenumber spectra are not in agreement with the model used by *Frankignoul and Müller* [1979] or *Müller and Frankignoul* [1981] which contains more small-scale (<5000 km) power than observed curl. Neither these studies nor those of *Brink* [1989] or *Samelson* [1989] completely include the observed east-west and north-south wavenumber asymmetries. Finally, *Chave et al.* [1991] showed that the spatial coherence structure of curl at a given frequency typically consists of a ≈1000-km-diameter main lobe and a number of more distant nonlocal peaks. This real feature of curl is not included in the simple parameterizations used in any of the cited studies, and might lead to under estimation of the coherent wind-forced response.

3. THE OBSERVATIONS

Electric Field Measurements

The oceanic response to atmospheric forcing is expected to be barotropic in the period range of interest (4–100 days) on the basis of both theory and prior observation. Conventional current measuring instrumentation is not ideal for measurement of barotropic currents since numerous current meters per mooring are required to differentiate the barotropic and baroclinic parts of the velocity field. Failure to separate the two components properly, and hence eliminate baroclinic noise, could result in underestimation of the barotropic velocity-to-atmospheric forcing coherence functions. Instead, techniques must be sought which offer direct measurements of the depth-averaged velocity. One such method which is now well established both theoretically and instrumentally is based on detection of the motionally induced horizontal electric field.

Chave and Luther [1990] present a recent theoretical investigation of motional electromagnetic induction, while *Sanford et al.* [1990] give a comprehensive overview of all aspects of the subject. These studies show that at low (subinertial) frequencies where the horizontal length scale of the flow is large compared with the water depth, the vertical velocity is small compared with the horizontal components, and the effect of self induction is weak, then the horizontal electric field to velocity relationship is given by

$$\mathbf{E}_h = C\, F_z\, \hat{z} \times \langle \mathbf{v}_h \rangle^* \tag{2}$$

where C is a dimensionless scale factor, F_z is the known vertical component of the geomagnetic field, and $\langle \mathbf{v}_h \rangle^*$ is the vertically integrated, seawater conductivity weighted horizontal water velocity. The latter may be understood by expressing the seawater conductivity in terms of its depth-averaged value $\langle \sigma \rangle$ plus a depth-dependent residual

$$\sigma(z) = \langle \sigma \rangle + \sigma'(z) \tag{3}$$

so that

$$\langle \mathbf{v}_h \rangle^* = \langle \mathbf{v}_h \rangle + \frac{\int_{-H}^{0} dz\, \sigma'(z)\, \mathbf{v}_h(z)}{H \langle \sigma \rangle} \tag{4}$$

where $\langle \mathbf{v}_h \rangle$ is formally the depth-averaged or barotropic velocity. For the BEMPEX area, *Luther et al.* [1991] used both historic average and contemporaneous experimental data to show that the second term in (4) contributes no more than 3% to $\langle \mathbf{v}_h \rangle^*$, so that the horizontal electric field is a direct measure of the barotropic velocity.

Other environmental factors which need to be considered when interpreting horizontal electric field data are discussed by *Chave and Luther* [1990] and *Luther et al.* [1991]. Electromagnetic noise from external, ionospheric and magnetospheric, sources is one potential complication. This type of noise becomes dominant only below 2-days period, and is not a significant problem for the present study at periods longer than 4 days based on prior observations [*Chave et al.*, 1989; *Luther et al.*, 1991]. Another environmental factor is electric current leakage into the poorly conducting seafloor as parameterized by C. *Chave and Luther* [1990] showed that C=0.95±0.05 for most points on the deep ocean floor based on indirect geophysical data. Since an independent calibration for C is not available, C will be set to 1 in the sequel. This will result in slight underestimation of the actual barotropic water velocity and has no effect on coherence analyses.

The self-contained, seafloor-based horizontal electrometers used in BEMPEX were proven instruments based on principles described by *Filloux* [1987]. The units record the electric potential across two orthogonal 6.3-m span salt bridges with a sampling rate of 16 per hour. They utilize an electromechanically activated electrode reversing technique to eliminate a large, time-variable electrode offset voltage as well as residual drift in the analog electronics. This ensures that all velocity measurements are referred to a true zero datum and remain accurate at the longest periods. For the BEMPEX area, the electrometers yield the horizontal velocity with a least count precision below 10^{-3} m s^{-1} without the rotor stalls which plague mechanical current meters in weak mean flows.

Experiment Location

The location of the BEMPEX array was chosen on the basis of a variety of sometimes conflicting scientific and practical criteria. First, it was deemed essential that atmospherically forced currents be (at a minimum) strong in winter. It was known from the work of *Niiler and Koblinsky* [1985] that this is true at 42°N, 152°W, and weather summaries suggested more intense atmospheric forcing to the north and west but not to the south

and east. A more comprehensive study subsequently published by *Koblinsky et al.* [1989] supported the choice of a more northerly and westerly site. As a second criterion, it was desirable to minimize the extent of mesoscale eddy activity that might be generated by processes other than atmospheric forcing (such as mean current instability) to ensure uncontaminated observations of the atmospherically forced barotropic currents by the electrometers. The surface eddy kinetic energy is especially low in the central North Pacific based on satellite altimetry [*Cheney et al.*, 1983], suggesting at most a weak instability-generated component in that region. Third, high latitudes were to be avoided since electromagnetic source field complications associated with the auroral zone might complicate removal of geomagnetic noise from the electric field data. In retrospect, this is not a significant issue, but uncertainties about the noise problem dictated a North Pacific site equatorward of ≈50°N. Fourth, high-amplitude, short-scale topography was to be avoided insofar as possible because of its tendency to introduce a variety of additional scales to the velocity field which might reduce the horizontal coherences. Finally, logistical constraints imposed by ship availability and the need for reasonable weather conditions during deployment and recovery precluded a site located too far north.

In the end, the BEMPEX array which was centered on 40°N, 163°W, with an 1100 × 1000 km aperture for all instruments is the result of several compromises. For example, there is quite a lot of short-scale topography, but only the organized structures associated with the Mendocino Fracture Zone which cuts through the southern portion of the array were thought to have sufficient amplitude to markedly alter the flow fields. As will become apparent, this is only partially true for the barotropic currents, but Luther et al. (1992) show that topography has essentially no effect on the pressure field. In fact, topographic effects have been treated as an opportunity, and the array was designed with the knowledge that the velocity field could be inhomogeneous such that only subsets of all of the array elements would be usable for wavenumber studies. The detailed

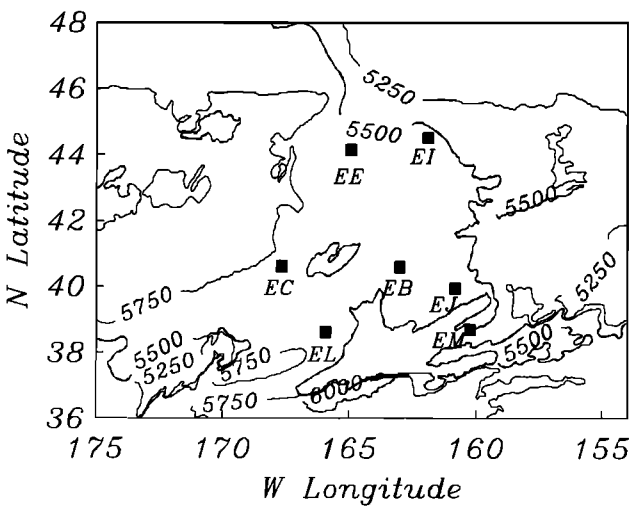

Fig. 1. Bathymetric map showing the locations of the seven horizontal electric field sites used in this study. The depth contours are taken from the ETOPO5 digital data base at 5' intervals. The principal bathymetric features in the BEMPEX area include the Mendocino Fracture Zone which strikes to the east-northeast at the bottom of the figure with EL and EM lying slightly to its north, the Surveyor Fracture Zone near the center of the map with an identical strike direction, and the Aleutian Abyssal Plain at the top of the figure.

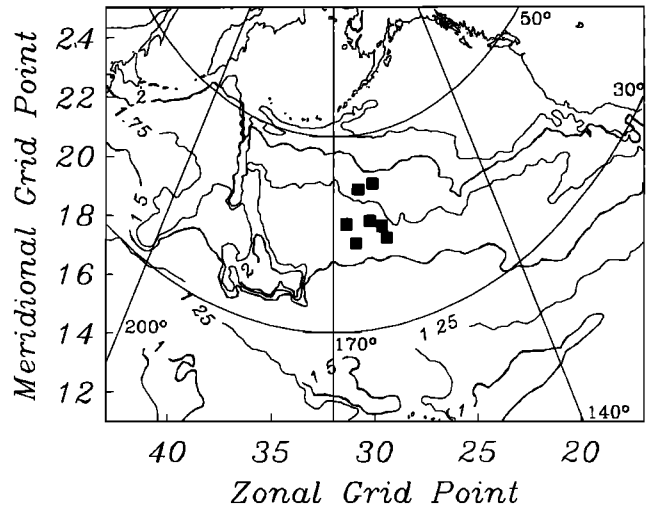

Fig. 2. Planetary component (f/H) of the potential vorticity computed from 1° averages of the ETOPO5 values. The contours are plotted on the FNOC polar stereographic projection with selected geographic isolines and the outlines (at top, from right to left) of North America, the Kamchatka Peninsula, Sakhalin Island, and Hokkaido, Japan. The abscissa and ordinate labels refer to the grid point designations used in the FNOC product. The seven BEMPEX horizontal electric field sites are shown at the center; see Figure 1 for instrument designations. The units of f/H are reciprocal meters per second scaled by 10^8.

array layout was based on the overriding concern that at a minimum, neighboring elements should be coherent at subinertial frequencies. This is a trivial requirement for the pressure field because of the observed and theoretical coherence scales of over 500 km [e.g., *Brown et al.*, 1975]. Less information was available for the current field, and conservative minimum spacings between electrometers of 150–300 km were selected. Finally, element locations were chosen to maximize the number of possible distinct spatial lags.

Figure 1 shows the locations of the seven barotropic current sites used in this study. The array was placed in a region of sediment-draped abyssal hills bounded on the south by the rugged Mendocino Fracture Zone, cut in the middle by the more subtle Surveyor Fracture Zone, and terminated to the north by the smooth Aleutian Abyssal Plain. The regional topography shoals gently to the northeast. Figure 2 is a larger scale map showing the electrometer sites superimposed on the dynamically important planetary vorticity (f/H) contours. For compatibility with the coherence maps discussed in section 5, this is depicted on a polar stereographic grid with selected geographic isolines and outlines of the continents added as an aid to the eye. The large-scale planetary vorticity contours slope to the east-southeast in the vicinity of the BEMPEX array. However, there is an abrupt shift to nearly meridional contours about 1500 km to the west which is caused by the Emperor Seamounts, many of whose constituents rise to within a few hundred meters of the sea surface.

Barotropic Velocity Data

Table 1 lists the identifiers, latitudes, longitudes, uncorrected water depths, and record lengths for the seven electrometer data sets. The nominal experiment length was 11 months, but one record (EB) is short at the beginning by about 30 days due to a water chopper seating problem which was self correcting. Of the remaining records, all are of the highest quality except for

TABLE 1. BEMPEX Electric Field Records

Site	N Latitude	W Longitude	Depth, m	Length, days
EE	44°8.9'	164°57.3'	5450	322.8
EI	44°31.3'	161°53.7'	5385	323.3
EC	40°37.1'	167°40.7'	5825	321.2
EB	40°35.8'	163°0.8'	5730	304.8
EJ	39°57.0'	160°48.7'	5550	322.2
EL	38°38.5'	165°56.2'	5575	323.2
EM	38°40.8'	160°13.7'	5365	321.8

EE, where one chopper channel showed evidence of a slow leak which reduced the amplitude of the solar daily variation by 15% over time. This was eliminated by scaling the data to equalize the amplitude of the solar daily variation as a function of time. All of the time series were rotated to geographic coordinates using the instrument orientations measured by an internal recording compass. The principal ocean tides as well as the solar daily variation and its first five harmonics were removed by robust least squares. The data were then low-pass filtered and decimated to 1- and 6-hour samples for subsequent analyses.

Figures 3 and 4 show the zonal and meridional barotropic currents as measured by the electrometers after further low-pass filtering to eliminate variability at periods shorter than 6 days, effectively removing any contamination by geomagnetic storms. The peak-to-trough amplitude is typically 1–2 cm-s^{-1} with occasional excursions of up to 4–5 cm-s^{-1}. Note the longer-period nature of the zonal component as compared to its meridional counterpart, especially for EJ, EL, and EM. The record from EB appears very similar in the two velocity components, reflecting strong circular polarization. Note also that the two northern records at EE and EI have a larger amplitude and somewhat lower frequency character than the remaining time series. There is also the suggestion of an annual cycle at most of the sites; this is especially apparent at EC and EJ. However, there is only weak visual evidence for a strong seasonal dependence to the higher-frequency fluctuations. For example, in the peak winter months during days 350 to 450, only the meridional velocity at EE and EI exhibits markedly stronger variability. This is quantified in Table 2, where the record variances for the low-passed data shown in Figures 3 and 4 are tabulated for the summer (July–September), fall (October–December), winter (January–March), and spring (April–June) periods. The variance range is typically a factor of 2 to 4. This is substantially smaller than the seasonal range for the curl variance, which exceeds a factor of 10 in the BEMPEX area [*Chave et al.*, 1991]. It is also much weaker than the decadal range in abyssal eddy kinetic energy observed in the eastern North Atlantic by *Dickson et al.* [1982] but is comparable to values given by *Koblinsky et al.* [1989] for two moorings to the west of the BEMPEX area. However, Koblinsky et al. quote a much larger seasonal range at other North Pacific sites, indicating that the BEMPEX array lies in a region of minimal seasonal variability.

The surface air pressure and wind field at 6-hour intervals were obtained at 405 locations over the North Pacific from the FNOC. *Brink* [1989] and other investigators cited by *Chave et al.* [1991] have demonstrated better consistency of the FNOC winds with direct observations than for different atmospheric products, so no others were investigated in detail. The wind velocity data were converted to wind stress estimates at 10 m height using Monin-Obukhov similarity theory and a velocity-dependent neutral drag coefficient. Curl was computed using a two-dimensional centered finite difference formula on a sphere, yielding 325 sites on a polar stereographic grid covering most of the North Pacific. Further details on treatment of the FNOC data are given by *Chave et al.* [1991].

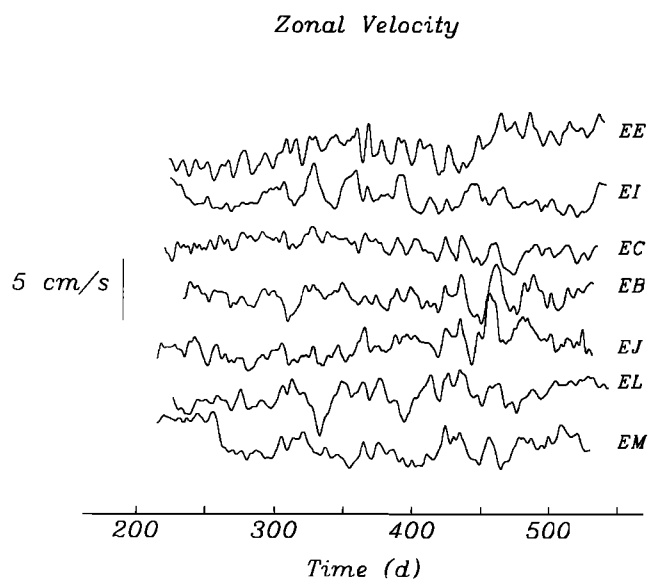

Fig. 3. Low-passed time series of the zonal velocity computed from (2) under the assumption that $C=1$ as described in the text. The prolate low-pass filter has a 3-dB point of 6 days with 60 dB of stop band attenuation. The time axis is in days from 0000 UT, January 1, 1986.

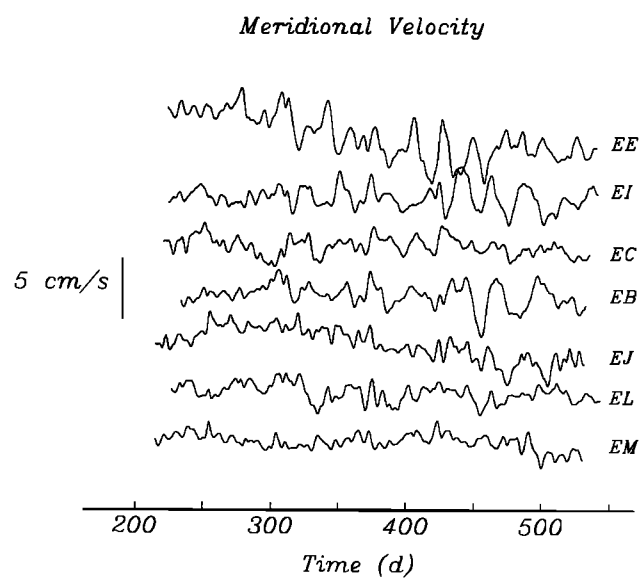

Fig. 4. Low-passed time series of the meridional velocity computed from (2) under the assumption that $C=1$ as described in the text. The prolate low-pass filter has a 3-dB point of 6 days with 60 dB of stop band attenuation. The time axis is in days from 0000 UT, January 1, 1986.

TABLE 2. Seasonal Variance

Site	Component	Variance, cm^2s^{-2}			
		Summer	Fall	Winter	Spring
EE	zonal	0.206	0.789	0.832	0.432
EI	zonal	0.563	0.873	0.669	0.491
EC	zonal	0.172	0.178	0.400	0.461
EB	zonal	0.267	0.469	0.638	0.999
EJ	zonal	0.351	0.417	0.696	1.259
EL	zonal	0.179	0.995	0.976	0.514
EM	zonal	1.068	0.435	0.653	0.658
EE	meridional	0.154	1.856	1.803	0.680
EI	meridional	0.235	0.559	1.069	1.013
EC	meridional	0.370	0.521	0.407	0.212
EB	meridional	0.136	0.401	0.942	1.224
EJ	meridional	0.718	0.251	0.415	0.640
EL	meridional	0.198	0.621	0.459	0.260
EM	meridional	0.157	0.128	0.236	0.491

4. BAROTROPIC CURRENT SPECTRA

All spectra in this paper are estimated using the multiple prolate window expansion introduced by *Thomson* [1982]. A multiple window spectrum is computed by first generating the natural set of orthogonal data windows (discrete prolate spheroidal or Slepian sequences) which are optimal in a minimum spectral leakage sense and which depend explicitly on the time-bandwidth product (resolution bandwidth times data series length). These windows are each applied to the time series as tapers prior to Fourier transformation, and since the windows are orthogonal, the raw estimates are approximately independent. The raw spectra are combined using a set of weights chosen to minimize broadband bias. The resulting spectrum is effectively the convolution of the unknowable true spectrum with a rectangular frequency domain window of width specified by the time-bandwidth product of the estimate. The multiple window approach results in a substantial increase in statistical efficiency compared with conventional band averaging while maintaining complete control of spectral leakage. However, the bandwidth of the estimate is independent of frequency, unlike for more conventional spectra. None of the conclusions presented here depend critically on the method of spectrum estimation, and all of the auto- and cross-spectral inferences discussed here can be verified using other (e.g., band averaging) techniques.

Figure 5 shows Cartesian and rotary power spectra for the barotropic velocity components at site EB located near the center of the BEMPEX array in Figure 1. The gross features, which are common to all of the seven sites, include a red spectrum (decreasing power with increasing frequency) at periods shorter than ≈0.5 day, a relative power maximum at 0.5-day period, and some residual power cusping near 24, 12, 8, 6, and 4.8 hours from inadequately resolved tides and the nondeterministic part of the solar daily variation. At periods longer than 1 day, there is a slight falloff in power to a relative minimum at periods of 2-3 days followed by a sharp rise toward low frequencies. As discussed in detail by *Chave et al.* [1989], horizontal electric field spectra are completely dominated by external sources at periods shorter than 1-2 days; the spectra in Figure 5 do not represent water velocities at periods below this point. The minimum in power at periods of 2-3 days and the rapid rise in power with increasing period beyond this are very similar in appearance to current meter spectra and are caused by motional electromagnetic induction [see *Luther et al.*, 1991].

Superimposed on the large-scale features in Figure 5 is a strong peak in both the zonal and meridional velocity centered at 20-to-50-day periods. The rotary spectra show this to be strongly counterclockwise polarized, and the peak width is

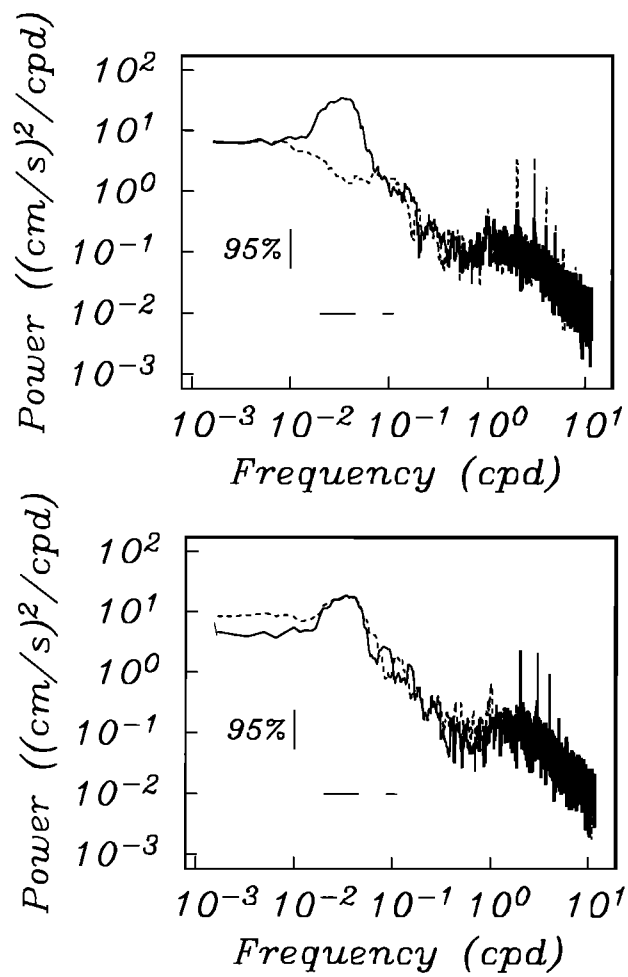

Fig. 5. Power spectra of the barotropic velocity at EB shown (top) in rotary form (counterclockwise=solid line) and (bottom) in Cartesian form (zonal component=solid line). The spectra were computed using the multiple prolate window method with a time-bandwidth of four and eight orthogonal windows, yielding about 16 equivalent degrees of freedom per frequency. The bandwidth of the estimate is 0.026 cpd, and the two horizontal bars indicate the bandwidth centered at periods of 30 and 10 days. The double-sided 95% confidence interval based on the χ^2 approximation is also shown.

somewhat wider than the resolution bandwidth. Additional, weak concentrations of variance appear in the zonal velocity at 10–14 and 6–8 days and in the meridional velocity at 8–10 days; these peaks are typically about 1 standard deviation high and are wider than the resolution bandwidth. There is only weak evidence for significant rotary effects outside the 20-to-50-day band. Note also that the zonal and meridional power is comparable at all periods, similar to the western North Atlantic observations of *Brink* [1989] . Integration of the 20-to-50-day peak yields an rms velocity of ≈0.5 cm-s^{-1}.

Figure 6 shows Cartesian and rotary spectra of the barotropic currents at EC, located at the western edge of the BEMPEX array in Figure 1. In contrast to site EB, the peak at 20–50 days is nearly absent, but as in Figure 5, weak spectral enhancements are apparent at 10–14 and 6–8 days, especially in the clockwise polarization, with peak widths that exceed the resolution bandwidth. Except for the 20-to-50-day band, the spectral levels at EB and EC are identical at all frequencies to within the statistical error of the estimate. However, the power at EB exceeds that at EC by a factor of 7 in the 20-to-50-day region.

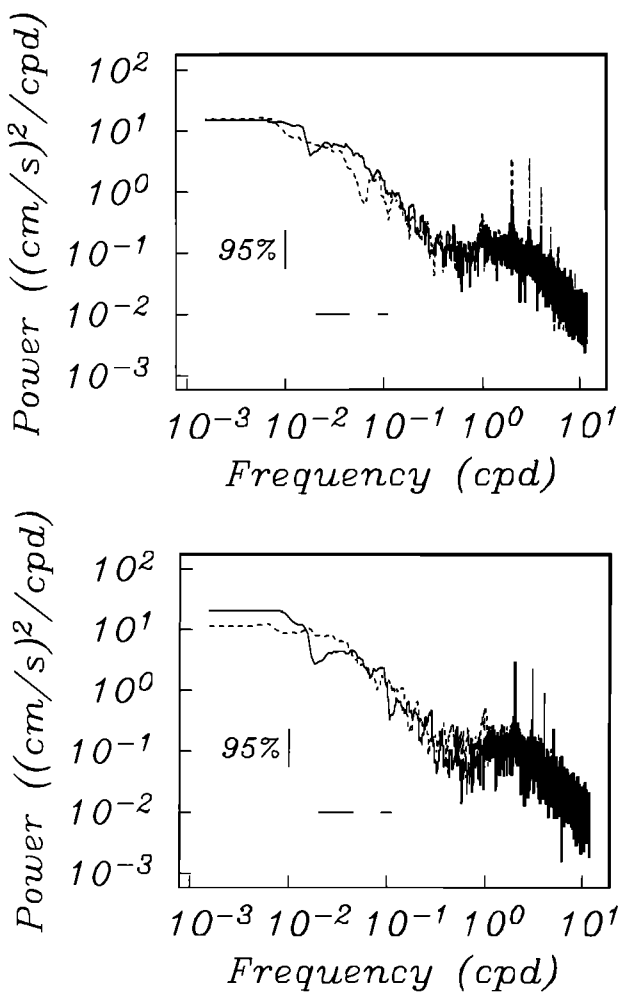

Fig. 6. Power spectra of the barotropic velocity at EC shown (top) in rotary form (counterclockwise=solid line) and (bottom) in Cartesian form (zonal component=solid line). The spectra were computed using the multiple prolate window method with a time-bandwidth of four and eight orthogonal windows, yielding about 16 equivalent degrees of freedom per frequency. The bandwidth of the estimate is 0.026 cpd, and the two horizontal bars indicate the bandwidth centered at periods of 30 and 10 days. The double-sided 95% confidence interval based on the χ^2 approximation is also shown.

The remaining five BEMPEX barotropic current sites yield spectra that are similar in behavior to EB or EC, with frequent if not ubiquitous occurrence of the spectral enhancements at 20–50, 10–14, and 6–8 days. For example, one of the two northern sites (EE) shows a strong 20-to-50-day peak in the meridional velocity, while EI displays a variance concentration with comparable zonal and meridional power over this band. There is no evidence for rotary polarization at either location. The spectrum is about a factor of 4 larger at EE than at EB for periods shorter than 20 days, and spectral peaks in that range are absent. However, at EI the peak at 10–14 days is quite apparent with moderate counterclockwise polarization, while the overall power is comparable to that at EB. At EJ, the 20-to-50-day and 10-to-14-day peaks are similar to those at EB in the Cartesian spectra, and counterclockwise polarization in the 20-to-50-day band is evident. At site EL, there is no apparent variance concentration except in the 10-to-14-day band, but the spectral level in the 20-to-50-day region is nearly as large as at EB. At site EM there is no evidence for weak spectral peaks and the spectral level is comparable to that at EL. For the latter two stations, the zonal power exceeds the meridional value by about a factor of 4 at periods longer than 20 days; for the remaining sites the spectra are essentially isotropic. Note that the weakly anisotropic velocity spectra are associated with the two sites nearest to the rough topography of the Mendocino Fracture Zone.

5. SPATIAL COHERENCE

It has been shown that curl fluctuates about zero wavenumber at periods longer than ≈10 days and displays increasing eastward and northward propagation at shorter periods at the BEMPEX latitude [*Chave et al.*, 1991]. As a zeroth-order demonstration that the ocean is impressing its own dynamics on the barotropic currents, it can be demonstrated that two-point cross spectra between pairs of barotropic velocity sensors consistently indicate westward phase propagation at all periods where the coherence is statistically meaningful, including periods shorter than 10 days. This is strongly suggestive of free Rossby waves at all periods that can reliably be studied; the coherence is quite small below 4 days owing to external geomagnetic noise.

Analysis Procedure

The spatial correlation of the barotropic currents and the atmospheric variables was studied by generating maps of the squared coherence (hereinafter simply coherence) between the electric field components and curl, zonal and meridional wind stress, and atmospheric pressure in both Cartesian and rotary form. In each instance, the coherence between a given oceanic velocity component and an atmospheric variable at each of 405 (325 for curl) North Pacific sites was computed using the multiple window method at a set of pre-selected periods. The resulting coherence values were then contoured on the polar stereographic grid on which the FNOC data were obtained (as shown in Figure 2) to avoid two-dimensional interpolation errors which can give false coherence peaks. A set of 15 overlapping period bands were chosen on the sometimes conflicting basis of adequately resolving phase variations while ensuring sufficient statistical reliability in the estimate. Table 3 lists the band center periods, time-bandwidth product (TBW), and lower/upper band limits assuming a 320-day record. It should be noted that the time-bandwidth of a spectral estimate is invariant under changes

TABLE 3. Period Bands for Analysis

Center Period	TBW	Upper Period	Lower Period
68	4	∞	37
38	4	72	26
25	4	36	19
19	4	25	15
15	4	18	13
13	4	16	11
10	4.5	12	9.1
8.9	5	10	7.8
7.4	6	8.6	6.5
6.3	6	7.1	5.6
5.4	7	6.1	4.8
4.7	8	5.3	4.2
4.0	9	4.5	3.6
3.5	10	3.9	3.2
3.1	11	3.5	2.8

in the record length and hence the bandwidth will vary slightly between instruments; this has little effect on the results discussed below given the values listed in Table 1. In all cases, the equivalent degrees of freedom is given approximately by $2\times(2\times\text{TBW}-1)$, and the coherence was contoured only if it exceeded zero at the 95% significance level based on this estimate. The two shortest period bands gave very weak and inconsistent results due to geomagnetic noise, and will not be considered further.

As an aside, it must be emphasized that the choice of bandwidth is critical toward gaining an accurate estimate of the coherence between the oceanic and atmospheric variables. The bandwidths listed in Table 3 represent minimum values and are much narrower than the three bands used by *Brink* [1989] or *Samelson* [1990] in their analyses of North Atlantic current meter data. For example, the three period bands used by Brink covered 76–23, 23–8, and 8–3.7 days, corresponding respectively to time-bandwidths of 9, 25, and 44 for his 600-day record length, substantially larger than the values listed in Table 3. As will be demonstrated, the coherences between barotropic velocity and the atmospheric variables are consistently 2–4 times larger in this study than in those of *Brink* [1989] or *Samelson* [1990]. While it might be tempting to ascribe this entirely to baroclinic noise contamination of the current meter data which were used by Brink and Samelson, it is possible that their wider bandwidths are also a significant factor. Comparing results for the time-bandwidths in Table 3 with Brink's larger values on the BEMPEX electrometer data consistently shows a reduction in coherence for the latter by at least a factor of 2 at a given frequency. This is not difficult to understand; in a free wave environment, the frequency and wavenumber bandwidths will be correlated, and wavenumber bandwidth is the primary determinant of coherence in the absence of significant measurement noise.

The ubiquitous tendency for the spatial correlation of curl to display multiple disconnected patches or teleconnections has been noted by *Chave et al.* [1991]. As a result, coherence between an oceanic variable and curl at a given point may be due either to a real relationship between the two variables or to a real correlation of the oceanic variable with curl at another point combined with an intercorrelation of curl with itself. This will be reflected in the occurrence of multiple spatial peaks in the coherence maps between barotropic currents and curl, sometimes making it difficult to elucidate the true forcing location(s). Such uncertainty will in many instances be resolvable by comparing the velocity-curl coherence maps with intercorrelation maps of curl at the candidate forcing location(s) with curl at all other North Pacific points. The intercorrelation map at the proper forcing location will mimic the original barotropic current to curl map. In some cases this procedure fails, and ambiguities may be further resolved by examining coherence maps between barotropic currents and the wind stress components or air pressure. Since significant coherence between these variables reflects coherence between curl and either wind stress or air pressure, coherence maps between curl at the candidate forcing location(s) and the relevant wind stress component or air pressure can be utilized to further localize the forcing site. Their utility in finding the correct forcing location is a major justification for computing maps of the barotropic velocity coherence with the wind stress components and air pressure. In general, the wind stress maps prove more discriminating than their air pressure counterparts due primarily to erratic coherence of the latter. Finally, in the presence of rotary polarization of the barotropic currents, rotary coherence maps prove to be essential in elucidating the true forcing location.

Figure 7 gives an example of the analysis procedure for the meridional velocity at EI at 7.4 days period. The lower left panel shows the meridional velocity-to-curl coherence which displays strong values centered on grid points 1834, 2324, and 1330 (where the first two digits refer to the meridional and the last two digits to the zonal grid coordinates), as well as several weaker patches. The remaining three panels show curl intercorrelation maps centered on 1834, 2324, and 1330 respectively, and it is clear that no single forcing location from among these three candidates unambiguously explains the data. The true location is easily deciphered by comparing the meridional velocity-to-zonal wind stress coherence map with the curl-to-zonal wind stress maps for the three candidate forcing locations. Figure 8 suggests that 2324 is the correct one since the upper right map in the figure is visually most similar to the lower left map. This conclusion is reinforced by the meridional wind stress (not shown) and by the air pressure maps (Figure 9). The procedure illustrated by Figures 7–9 has proven very useful in the present study. However, it should be emphasized that there is no guarantee that it will always work since there may very well be more than one forcing location at a given period for a given sensor. In this instance, the problem becomes a more subjective exercise in pattern matching with a consequent rise in uncertainty.

As an aside, it might be expected that with either 325 or 405 sites distributed across the North Pacific, random chance would produce coherence above the 95% significance level at 1 in 20 of them that could be confused with real forcing. There are a number of problems with this argument. First, the FNOC product is heavily spatially smoothed, and hence there are substantially fewer independent estimates of the atmospheric variables. Quantification is difficult because the smoothing is data dependent. Second, the distribution of coherence in space between the oceanic velocity and curl at a given frequency is clearly not Gaussian because the spatial distribution of curl is itself not Gaussian, as witnessed by the presence of multiple disconnected peaks in its spatial autocorrelation function. Finally, random coherence would be expected to appear as small disconnected patches rather than the more spatially extended, contiguous ones that are typically observed. Given the statistical complexity and concomitant difficulty in quantifying significance tests, a conservative approach is taken in the sequel. No coherence estimate

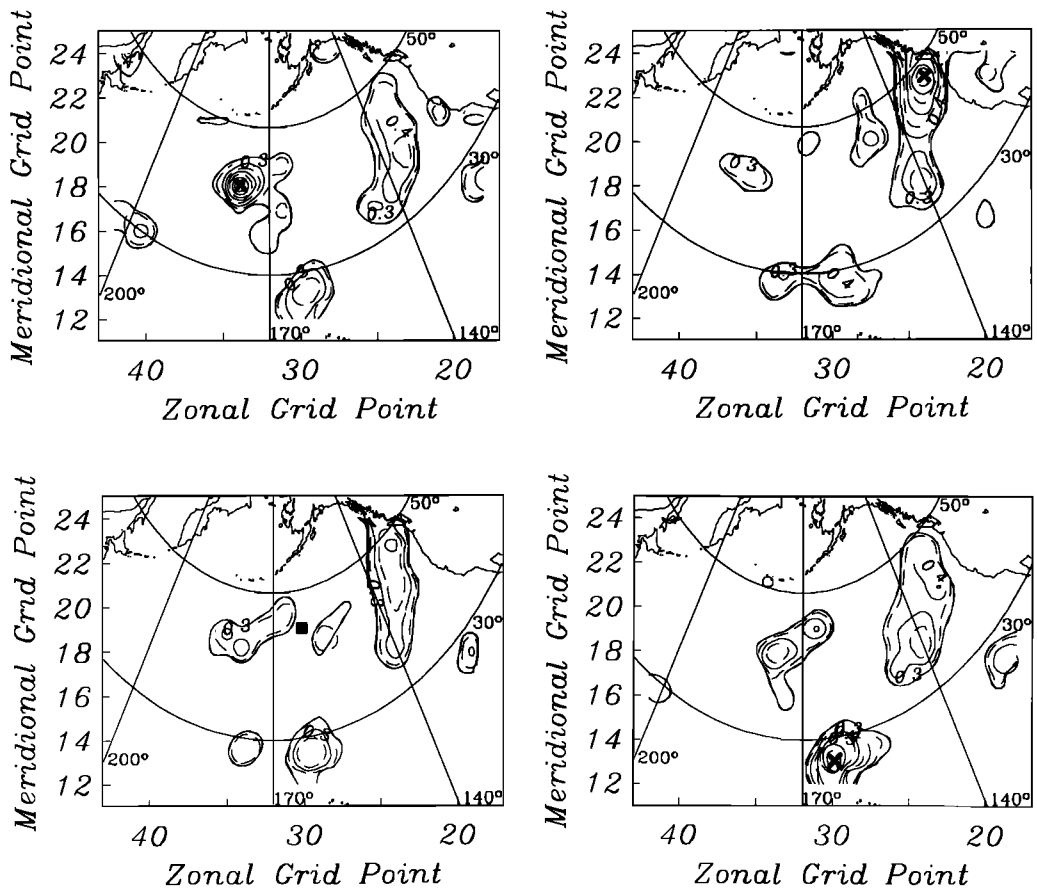

Fig. 7. The bottom left panel shows the squared coherence between the meridional velocity at EI and curl throughout the North Pacific at 7.4-days period, which peaks at 0.60 at grid point 2324 located off of northwestern North America. Other strong peaks are observed, notably at grid points 1834 with a coherence of 0.47 and 1330 with a coherence of 0.57. The solid square shows the location of EI. From the top left and proceeding clockwise, the remaining panels show the coherence of curl with itself centered respectively at grid points 1834, 2324, and 1330; the coherence is 1.0 at those points by definition. Contours of the squared coherence are shown beginning at the zero coherence level at 95% significance of 0.25 (heavy line) and at intervals of 0.1 starting at 0.3, with odd contours shown as dashed and even contours shown as solid lines. Note the similarity of all three curl intercorrelation diagrams with the current-curl coherence, reflecting strong atmospheric teleconnections.

is taken seriously unless it is well above the 95% significance level for two-point coherences and displays a well-formed coherent patch. In addition, assertions based on the barotropic velocity to curl coherences are always backed up by strong coherences between velocity and the remaining atmospheric variables.

As a further aside, the general consistency of the velocity-to-air pressure coherence maps with the velocity-to-curl coherence maps when the former are strong (for which Figures 7 and 9 are a good example) is further evidence that surface air pressure forcing of the ocean is unimportant. If significant forcing by air pressure were present, then this would represent an additional process in the velocity-to-air pressure maps which would alter the spatial patterns and destroy the agreement.

In the remainder of this section, the evidence for atmospheric forcing in the BEMPEX barotropic current data will be presented. The analysis procedure outlined above is always applied, but in most cases the details on how the correct forcing location is deduced will be omitted. Note that this requires considerable computation; in all, several thousand coherence maps have been generated. To anticipate the results somewhat, note that coherence between the barotropic velocity sensors and atmospheric forcing is nearly ubiquitous, but the spatial patterns are often variable. Typically, but not always, the strongest coherence is observed between the barotropic velocity and curl, with somewhat weaker results for the wind stress components and especially for air pressure. This is surprising given the expected reduced noise level in the air pressure and wind stress data, but probably reflects the relative wavenumber bandwidths; *Müller and Frankignoul* [1981] predicted stronger local coherence at long periods for barotropic meridional velocity with curl than for the remaining atmospheric variables. With 7 sensors and 15 frequency bands, it is not possible to illustrate all of the features of the coherence maps, and only selected highlights will be shown. A more complete description is available from the authors for comparison with atmospheric forcing models, including complete coherence maps. For convenience, the 15 frequency bands will be divided into three groups to facilitate description and discussion. This is not meant to imply that the three atmospheric forcing regimes discussed in section 2 should be identified with the three groups.

Long-Period (68–19 Days) Group

The long-period group (i.e., estimates centered on 68, 38, 25, and 19 days) is characterized by considerable uniformity at a

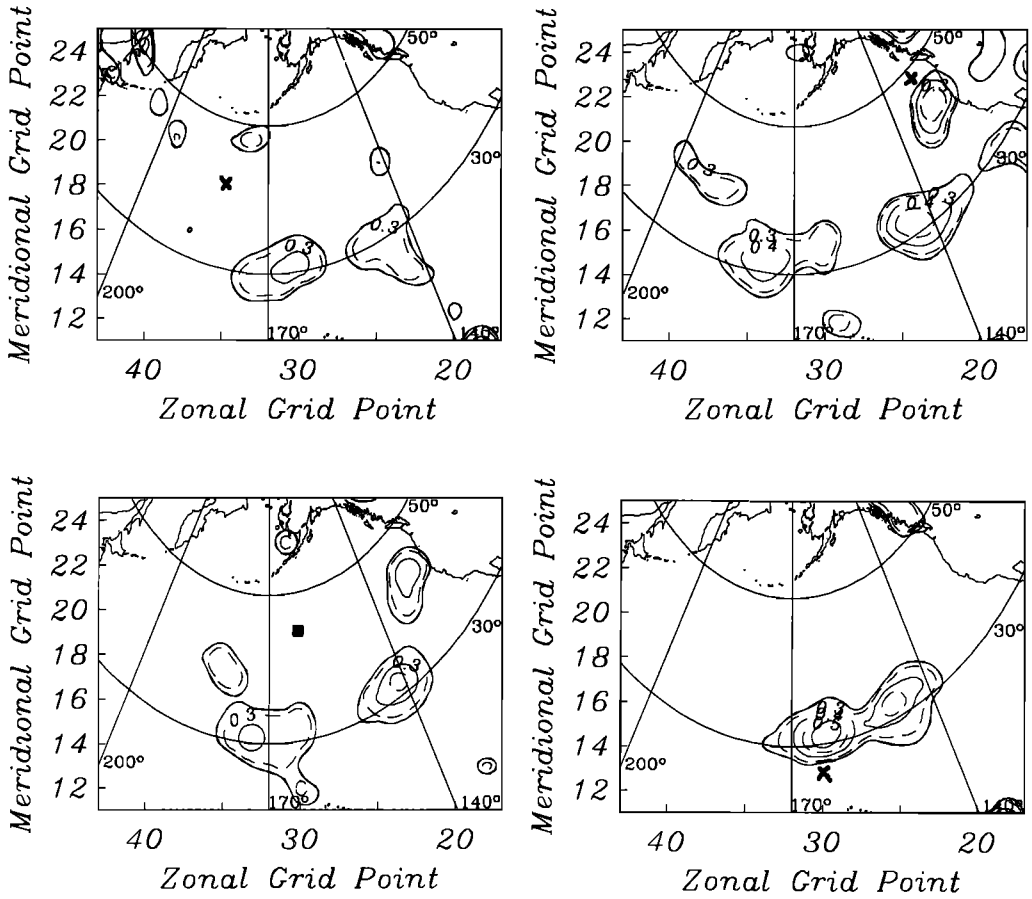

Fig. 8. The bottom left panel shows the squared coherence between the meridional velocity at EI and the zonal wind stress throughout the North Pacific at 7.4-days period. The solid square shows the location of EI. From the top left and proceeding clockwise, the remaining panels show the coherence of curl respectively at grid points 1834, 2324, and 1330 with zonal wind stress. Contours of the squared coherence are shown beginning at the zero coherence level at 95% significance of 0.25 (heavy line) and at intervals of 0.1 starting at 0.3, with odd contours shown as dashed and even contours shown as solid lines. Note that the 2324 curl diagram matches the current-τ_x coherence, suggesting that it is the true forcing location from among the candidate sites shown in Figure 7.

single site for each of the four period bands, but with some intersite variability. The single exception to these generalities occurs for the gravest band (68 days) which shows especially strong intersite differences, probably reflecting the wide frequency (hence wide wavenumber) bandwidth and the presence of multiple processes. While the data are nonlocally coherent with curl for 68 days at all sites save EB, there is almost no similarity between sites for a given barotropic velocity component, and confusion from curl intercorrelation is especially severe. However, it is of interest to note that local coherence with curl occurs for EL (zonal), possibly reflecting a topographic Sverdrup balance.

The next two bands (38 and 25 days) show very strong pattern similarities at about half of the sites. At 38 days, a double-lobe pattern reminiscent of the *Brink* [1989] result is clearly established for the zonal velocity at EC and EJ and for both velocity components at EB. The latter reflects the strong rotary polarization seen in Figure 5. Local coherence is also established for EC (meridional), making it the only site which exhibits all of the gross characteristics of the Brink model (Figure 10). Note that the northeast zonal patch is nearly in phase, the southeast zonal patch is nearly out of phase, and the local coherence for the meridional component is approximately in quadrature. There is a slight clockwise rotation of the double-lobe in Figure 10, in rough accordance with the orientation of the planetary vorticity contours in Figure 2. Unlike at EC, EJ (meridional) is incoherent.

At 25 days, the double-lobe pattern at EC, EB, and EJ is slightly stronger and appears in addition at EM (zonal). A new coherent patch is also seen to the northwest of the stations for the zonal component which is due to curl intercorrelation. However, EM (meridional) is forced from about 1200 km to the south, contrary to the Brink model, while EJ (meridional) is weakly coherent with a point far to the southeast. EC (meridional) continues to be locally coherent. Based on the analysis of curl, wind stress, and air pressure coherences described earlier, it is not possible to show that either the northeast or southeast patch in the zonal double-lobe pattern is the sole forcing location at either 38 or 25 days. This conclusion derives from the strong curl coherence that the northeast lobe shows with the southeast one, and vice versa. Two forcing points clearly must be present for some sites; note that, for instance, two phase-locked waves in quadrature are required to produce the strong counterclockwise circular polarization at EB (Figure 11) and the counterclockwise elliptical polarization at EJ. In addition, the northeast forcing point remains fixed at grid points 2026–2027 for both 38 and 25 days at all stations, while the southeast one shows slight spatial variability between sites and

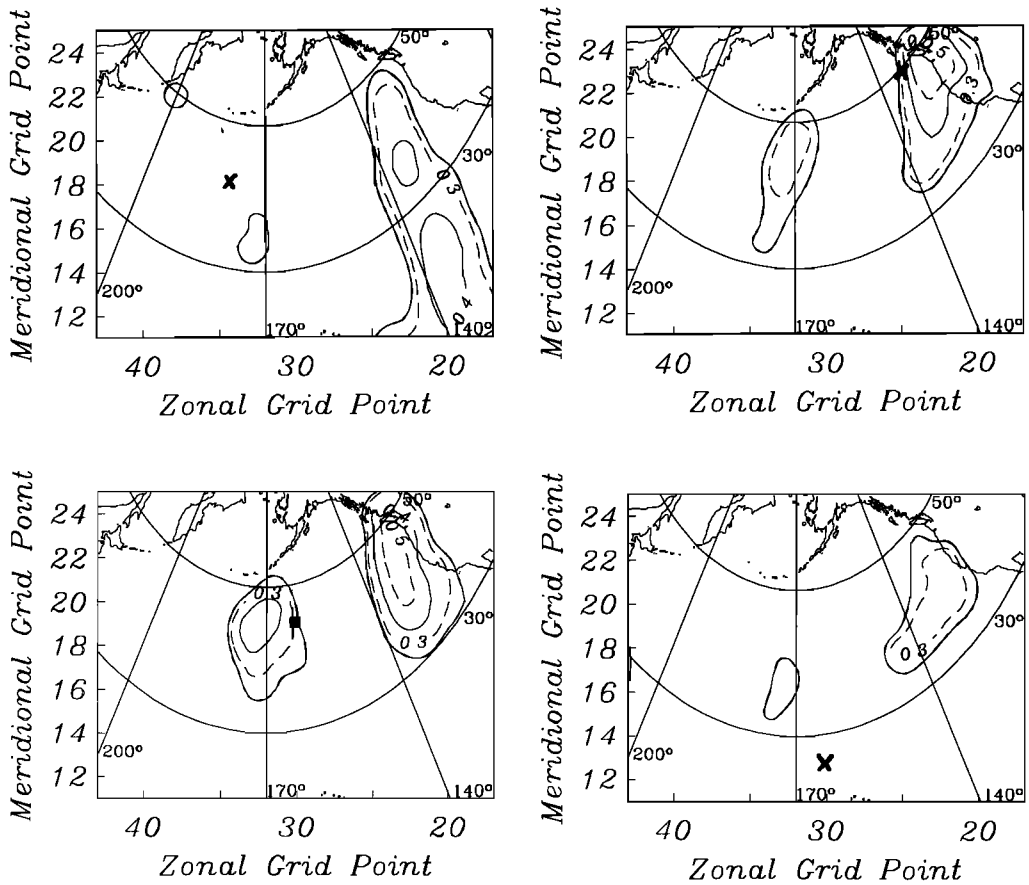

Fig. 9. The bottom left panel shows the squared coherence between the meridional velocity at EI and the surface air pressure throughout the North Pacific at 7.4-days period. The solid square shows the location of EI. From the top left and proceeding clockwise, the remaining panels show the coherence of curl respectively at grid points 1834, 2324, and 1330 with air pressure. Contours of the squared coherence are shown beginning at the zero coherence level at 95% significance of 0.25 (heavy line) and at intervals of 0.1 starting at 0.3, with odd contours shown as dashed and even contours shown as solid lines. Note that the 2324 curl diagram matches the current-air pressure coherence, suggesting that it is the true forcing location from among the candidate sites shown in Figure 7.

especially between the two periods. The rotation of the double-lobe pattern seen in Figure 10 is somewhat visible in Figure 11, but a substantial northward displacement of the seafloor station relative to the pattern is more apparent. The rotation phenomenon and station displacement is variable between the sites, probably reflecting local topographic effects.

These examples should not be taken as an indication that the evidence for atmospheric forcing is weak in the remaining data sets for 38 and 25 days; in fact, they are almost always significantly coherent with curl. Pattern similarities between stations are more elusive and the patterns typically change between frequencies for a given site. However, EL (zonal) is locally coherent at 38 days, as it was for 68 days. While local coherence is also suggested at 25 days, the actual forcing location at this period has been determined to lie ≈1500 km to the northwest.

The remaining long period band (19 days) shows fewer persistent patterns and the relation between barotropic velocity and curl, wind stress, and air pressure is more confused. In particular, the double-lobe pattern in the zonal component at EC, EB, EJ, and EM is absent. Nevertheless, the coherence between velocity and curl is typically strong. For example, the zonal component is forced from the distant southeast (grid points 1521–1523) at EI, EC, EB, and EJ (Figure 12 shows EC as an example). Intersite variability in the forcing location for the meridional velocity is more substantial, and no clean patterns are discernible. The apparent local coherence seen at 68–25 days in EL (zonal) is gone, but EL (meridional) is coherent immediately to the north of the station. It is possible that the 19-day band is transitional between the strong patterns at 38–25 days and the equally intense 13-day patterns described below. Note that at many of the sites, 38 and 25 days straddle the peak in power described in section 4, while 19 days lies at a point of weaker variability.

Intermediate-Period (15–8.9 Days) Group

The intermediate-period group (i.e., the 15-, 13-, 10-, and 8.9-day bands) displays a multitude of different coherence patterns and covers a gross transition from distant to more localized forcing. Like the 19-day band, the 15-day band displays few common patterns and is quite confused compared to the 38-to-25-day region. The overall coherence is typically lower than for the 19-day band. This is especially true for the zonal velocity, which is nearly incoherent with curl at EE, EI, EC, EB, and EM. However, EJ (zonal) and EL (zonal) are strongly coherent (>0.7) with curl, having an inferred forcing location ≈2000 km to the southwest of the two stations. The meridional velocity is even more variable between sites, with nearly local coherence at some places and east or west forcing at others. In

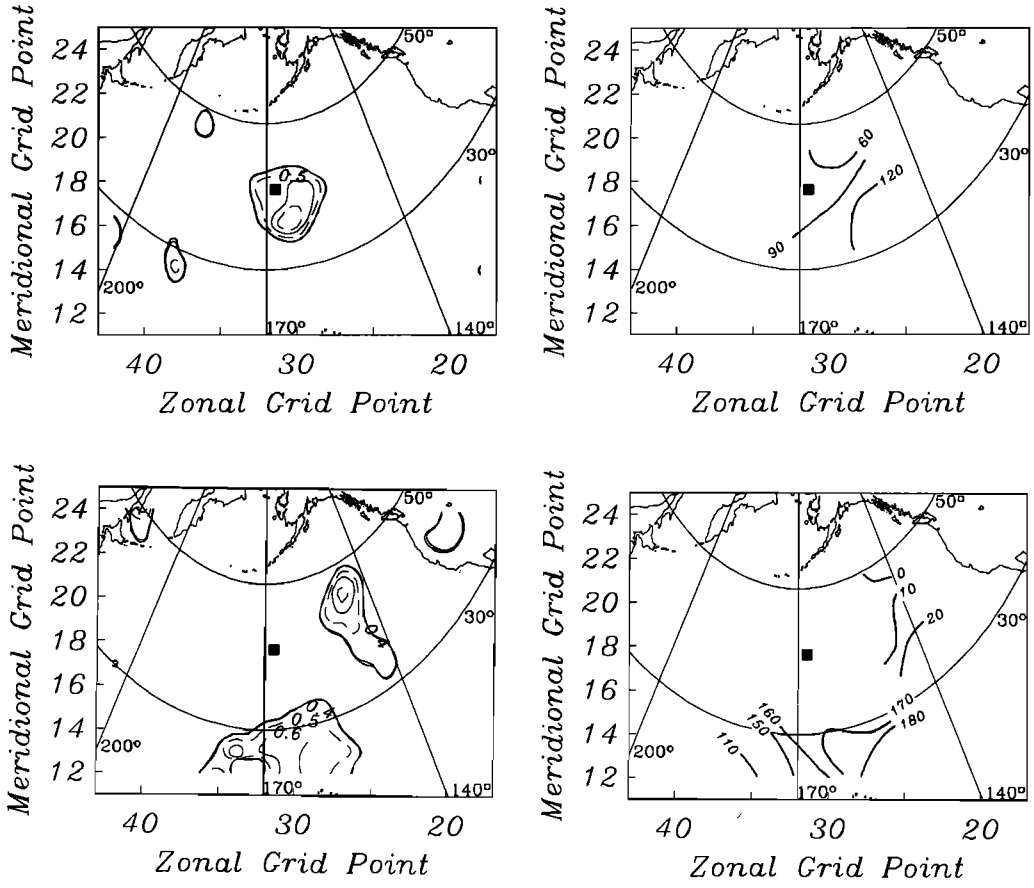

Fig. 10. Maps of (left) squared coherence and (right) phase between the (top) meridional and (bottom) zonal barotropic velocity at EC and curl over the North Pacific at a period of 38 days. The location of EC is shown as a solid square. Coherence contours are shown beginning at the zero coherence level at 95% significance of 0.39 (heavy line) and at intervals of 0.1 starting at 0.4, with odd contours shown as dashed and even contours as solid lines. The peak coherence for the zonal velocity is 0.72 at the northeast lobe (grid point 2027) and 0.68 at the southeast lobe (grid point 1230), while the meridional coherence is 0.75 just to the south-southeast (grid point 1631) of the sensor. A positive phase means that curl leads the barotropic velocity.

addition, the strong counterclockwise polarization seen in the 20-to-50-day range for EB is replaced by clockwise polarization, while other rotary effects vanish.

A new and persistent pattern is established at 13 days for all sites save EM; note that this band is located near the center of a persistent, weak spectral peak as described in section 4. The zonal velocity is clearly forced from the east-northeast at a distance of ≈1500 km, as is illustrated for EL in Figure 13. In contrast to 38 days (Figure 10), the forcing point is nearly in quadrature. The forcing location is identical for all sites, and the coherence exceeds 0.7 at EE, EC, EB, and EL. In addition, a nearly local curl intercorrelation is apparent, as can be seen in Figure 13. The zonal current coherence pattern also appears for the meridional velocity at EE and EC, but there is no evidence for rotary motion, while the remaining meridional components are incoherent with curl. EB (zonal) shows an additional southeast lobe (Figure 14), reflecting rotary polarization where the counterclockwise velocity-to-curl coherence is nearly identical to the zonal one. The phase at the northeast lobe is comparable to that for EL (Figure 13) and the southeast one is ≈180° different. However, unlike at 38 and 25 days, curl at the northeast lobe is not coherent with that at the southeast patch. The pattern seen at five of the six sites is qualitatively like that predicted by *Samelson and Shrayer* [1991], where a northward increase in curl power included in the *Samelson* [1989] model removed the southeast zonal coherence lobe. Local coherence between meridional velocity and curl is not observed for any of the sensors.

The coherence at 10 days takes the form of multiple, small-scale, scattered patches which sometimes make it difficult to deduce the forcing locations. In some instances, it appears that multiple forcing sites are required to explain the data since little consistency is observed in the coherences between velocity and curl, wind stress, and air pressure. In addition, the diameter of the coherent patches approaches the FNOC cell size, making it likely that the coherence is biased or even spatially aliased by the inherent smoothing in the wind product. However, there is some tendency for north-northeast nonlocal forcing of the zonal component and weak local coherence of the meridional component in which the patch is displaced to the north of the station. Figure 15 shows EJ, a particularly clean example. This resembles the short period patterns in *Samelson and Shrayer* [1991], although the size of the forcing region is smaller than in the model. While the small size of the forcing region might be regarded as of dubious significance, the connection to the atmosphere is both strong and spatially-extended for the remaining atmospheric variables, especially the zonal wind stress.

There is an increasing tendency for northern and western forcing locations at 8.9 days. The zonal velocity is driven from different points slightly north of the sensor at three sites (EE,

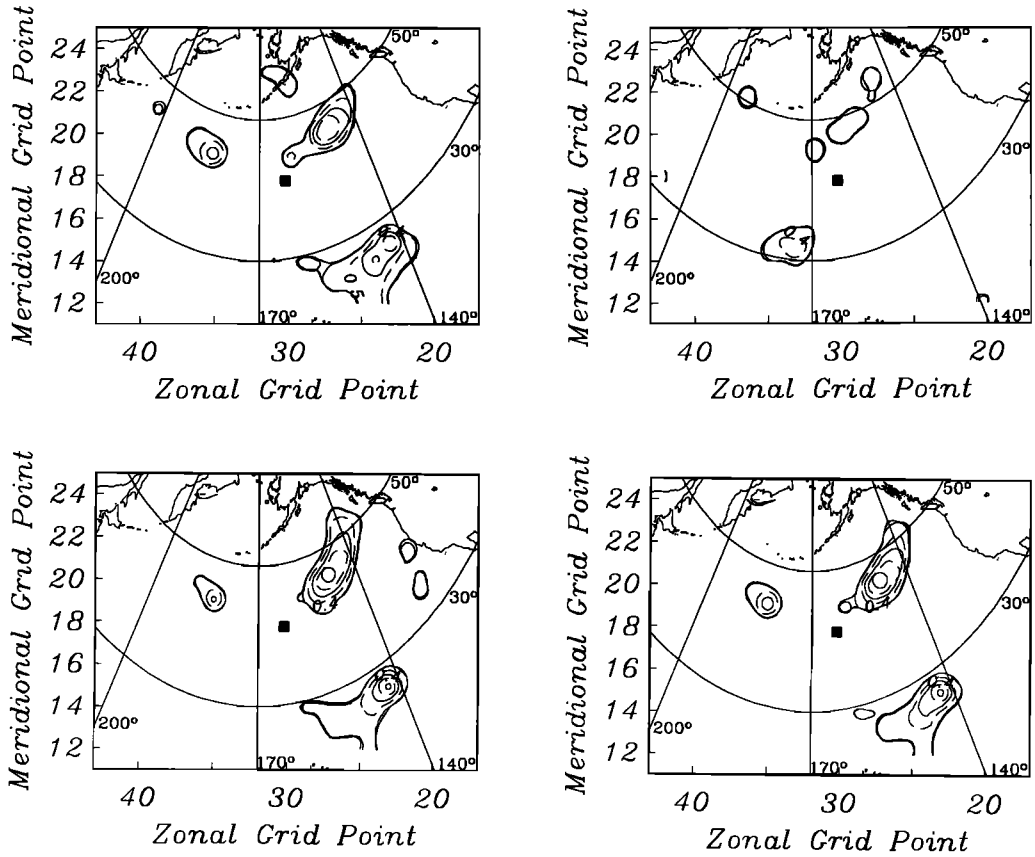

Fig. 11. Maps of the squared coherence between the barotropic velocity at EB and curl over the North Pacific at a period of 25 days. The left panels show the coherence between the (top) meridional and (bottom) zonal velocity and curl, while the right panels show the coherence between the (top) clockwise and (bottom) counterclockwise velocity and curl. The location of EB is shown as a solid square. Coherence contours are shown beginning at the zero coherence level at 95% significance of 0.39 (heavy line) and at intervals of 0.1 starting at 0.4, with odd contours shown as dashed and even contours as solid lines. The peak coherence for the zonal and counterclockwise velocity is 0.81 at grid point 2027.

EB, and EJ) and is strongly (γ^2>0.75), locally coherent at EM, but EC and EL display more distant forcing in the west. The meridional current forcing point appears to be more variable in azimuth, with a nearby northern forcing location for EE and EC, a southern forcing location at EI and EB, a western forcing location at EJ and EL, and a northeastern forcing location at EM. Figure 16 shows coherence maps for EJ, illustrating both nearby, northern coherence for the zonal component and more distant, western forcing for the meridional one.

Short-Period (7.4–4 Days) Group

The short period group (i.e, the 7.4-, 6.3-, 5.4-, 4.7-, and 4.0-day bands) displays stronger meridional and weaker zonal coherence with curl as period decreases. It also consistently shows a tendency for more localized to western forcing locations, and eastern forcing locations become less frequent. The single exception to this is at 7.4 days, where a very strong, meridionally elongate forcing pattern for the meridional velocity centered off of the northwest coast of North America (e.g., Figure 7) is seen at all of the sites except EE. This band is located at the center of a weak spectral peak as described in section 4. The inferred forcing point is variable between the sites, ranging north-south over about 1000 km. Figure 17 shows the pattern for EB, which demonstrates the intersite consistency by comparison with Figure 7. The most extreme pattern difference appears at the two southern sites, especially EL where the strongest coherence appears south of that in Figures 7 and 17. The coherence for all six sensors (except EE) is typically in excess of 0.5. While a weak western coherent patch is present for some of the sites, it is absent at EB (Figure 17), and an eastern forcing location is completely consistent for curl, the wind stress components, and air pressure (Figures 7–9). The corresponding zonal current coherences are generally weaker without a common pattern between sites. Some of the zonal currents are either locally coherent or incoherent, while the remainder appear to be forced from a distant southeast point.

The common pattern observed at 7.4 days vanishes for the 6.3 day band, and a large amount of intersite variability is seen, as at 8.9 and 10 days. However, coherence between the barotropic velocity and curl remains strong. The interstation variability is larger for the zonal component, ranging from local coherence to nonlocal coherence to the south and southwest when significant. A weak pattern is seen for the meridional velocity, where three locations (EE, EI, and EC) are forced from the same southwest point at ≈800 km range. Figure 18 illustrates this for EC. The remaining sites are either incoherent or forced from different, more distant eastern points.

At 5.4 days, the intersite variability remains large but there is a tendency toward local coherence for the meridional component. There is also the beginning of a general reduction in

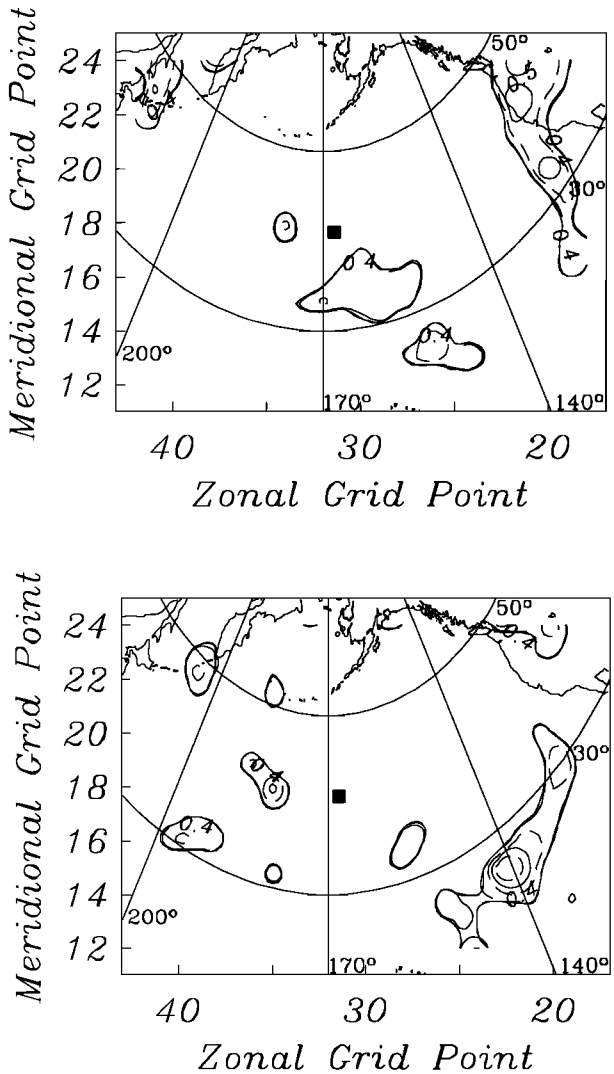

Fig. 12. Maps of the squared coherence between the (top) meridional and (bottom) zonal barotropic velocity at EC and curl over the North Pacific for a period of 19 days. The location of EC is shown as a solid square. Coherence contours are shown beginning at the zero coherence level at 95% significance of 0.39 (heavy line) and at intervals of 0.1 starting at 0.4, with odd contours shown as dashed and even contours as solid lines. There is strong counterclockwise polarization at this site, so the two velocity components are not independent. The peak coherence for the zonal and meridional components is 0.77 at a phase of ≈160° (grid point 1522) and 0.69 at a phase of ≈−40° (grid point 2020), respectively.

coherence due to external geomagnetic noise. No clear pattern is seen for the zonal velocity, and forcing from all azimuths is apparent, but all sensors save EC are coherent. However, the meridional velocity is locally coherent at four sites (EE, EI, EB, and EM), with the remaining sensors either incoherent or forced from the east. Figure 19 illustrates strong local coherence for both velocity components at EE.

The 4.7- and 4-day bands continue to show a weak preference for more localized or western coherence, but it is increasingly difficult to infer the correct forcing location, probably due both to the presence of more than one forcing location and to a rising relative noise level. There is a weak tendency toward a more western bias of the local forcing region when local coherence exists. Figure 20 shows a particularly clean example from EB (meridional) which should be compared with Figure 19.

Summary

A number of key observations have been made, and it is useful to summarize them. First, strong coherence of the barotropic currents with curl at some point is the rule rather than the exception. In the rare instances where those quantities are uncorrelated, evidence for coherence between the currents and wind stress or air pressure invariably is present. The coherence is more often nonlocal than local, although there is a tendency for increasingly nearby coherence with marked azimuthal scatter as the period decreases.

Second, the peak squared coherence of barotropic velocity and curl is typically ≈0.6 outside of the short period bands where geomagnetic noise degrades the result. For some bands and sensors, the peak squared coherence may rise up to 0.8, and it is rare for it to fall below 0.4. This should be contrasted with previous studies, where peak squared coherences of less than 0.2 were the rule [*Brink*, 1989; *Samelson*, 1990].

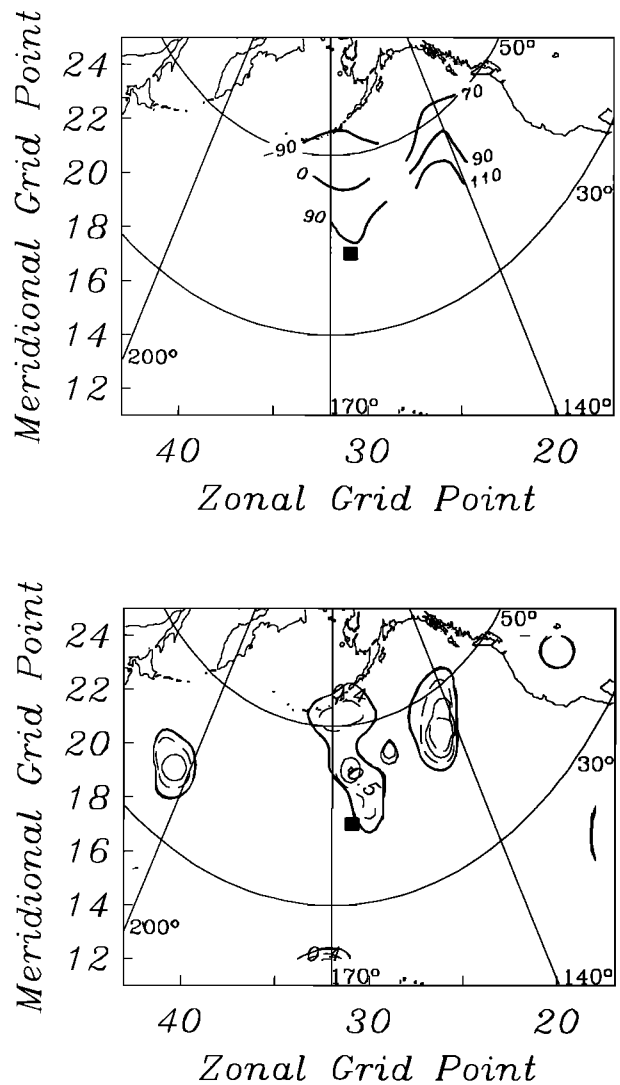

Fig. 13. Maps of the (top) phase and (bottom) squared coherence between the zonal barotropic velocity at EL and curl over the North Pacific for a period of 13 days. The location of EL is shown as a solid square. Coherence contours are shown beginning at the zero coherence level at 95% significance of 0.39 (heavy line) and at intervals of 0.1 starting at 0.4, with odd contours shown as dashed and even contours as solid lines. The peak coherence at grid point 2026 is 0.79. A positive phase means that curl leads the barotropic velocity.

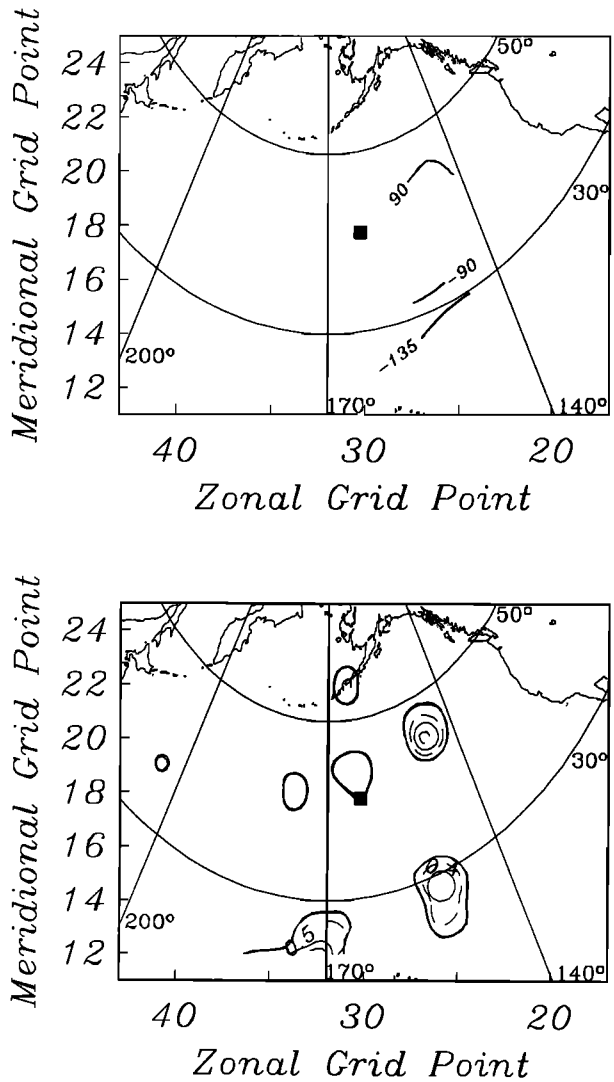

Fig. 14. Maps of the (top) phase and (bottom) squared coherence between the zonal barotropic velocity at EB and curl over the North Pacific for a period of 13 days. The location of EB is shown as a solid square. Coherence contours are shown beginning at the zero coherence level at 95% significance of 0.39 (heavy line) and at intervals of 0.1 starting at 0.4, with odd contours shown as dashed and even contours as solid lines. The peak coherence at the northeast peak (grid point 2027) is 0.73, while that at the southeast lobe (grid point 1526) is 0.63. A positive phase means that curl leads the barotropic velocity.

Third, strong spatial coherence patterns are observed at multiple sensors only in the 38, 25, 13, and 7.4 day bands. In two instances (13 and 7.4 days), six out of seven sensors display similar patterns. It should be noted that these bands all coincide with weak power spectral enhancements at many of the sites. There is some qualitative agreement of the coherence patterns with the nonlocal model predictions. More tenuously, there is evidence for a westward shift of the zonal, nonlocal, northeast coherent patch to the west with period until it lies directly north of the ocean observer, which is in qualitative agreement with the *Samelson and Shrayer* [1991] model.

Fourth, the pattern diversity observed between stations at a given period outside of these bands is remarkable, and abrupt changes with period for a single sensor appear to be the rule. As an example of the latter, consider the zonal velocity at EI starting at the longest periods. The forcing point is from the east-southeast at a distance of ≈3000 km combined with one or two less distant south and south-southwest locations (38 days); from the same east-southeast point (25 days), from a south-southeast point 3000 km distant (19 days); from a different, nearby point (15 days); from the east-northeast at a distance of ≈1400 km (13 days); from the west at ≈2000 km range (10 days); from the southwest at ≈2000 km combined with a more distant western point (8.9 days); from the far southeast at ≈3000 km range (7.4 days); indeterminate because of weak coherence (6.3 days); from the southwest at a distance of ≈3300 km (5.4 days); from the east and south at multiple points (4.7 days); and from the east at a distance of ≈2500 km (4 days). This example is not unusual.

Fifth, rotary polarization is observed at some sites for some bands. For the 20-to-50-day band, counterclockwise circular polarization is dominant at EB and is weakly present at nearby

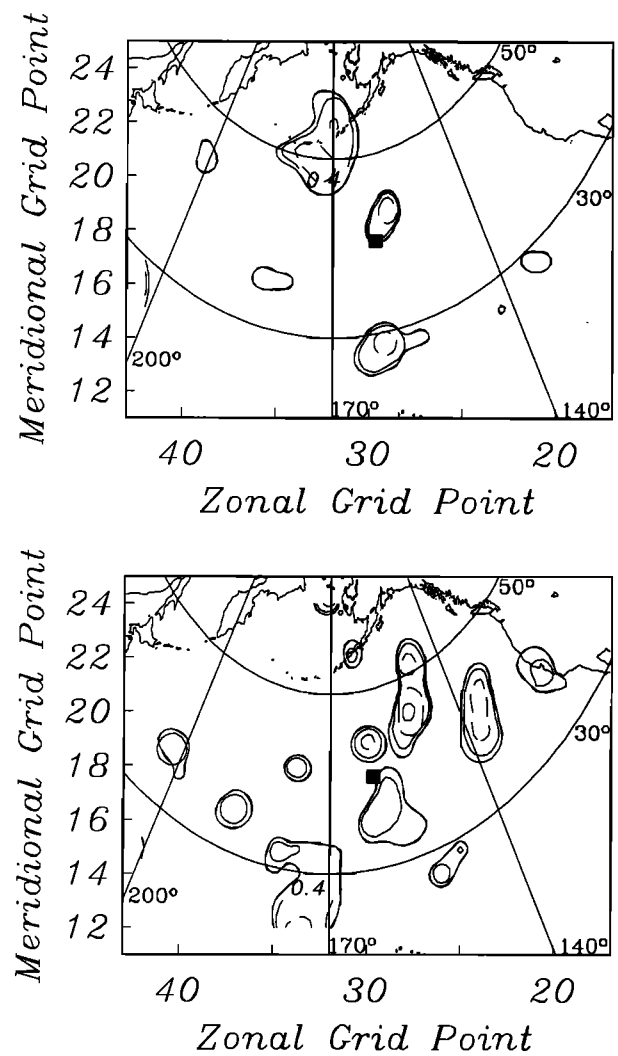

Fig. 15. Maps of the squared coherence between the (top) meridional and (bottom) zonal barotropic velocity at EJ and curl over the North Pacific for a period of 10 days. The location of EJ is shown as a solid square. Coherence contours are shown beginning at the zero coherence level at 95% significance of 0.35 (heavy line) and at intervals of 0.1 starting at 0.4, with odd contours shown as dashed and even contours as solid lines. The zonal velocity is forced from grid point 2028, where the coherence is 0.63 and the phase is ≈-90°. The meridional velocity is locally coherent at the south edge of a patch centered on grid point 1929, where the coherence is 0.59, although there may be some additional forcing from grid point 2033.

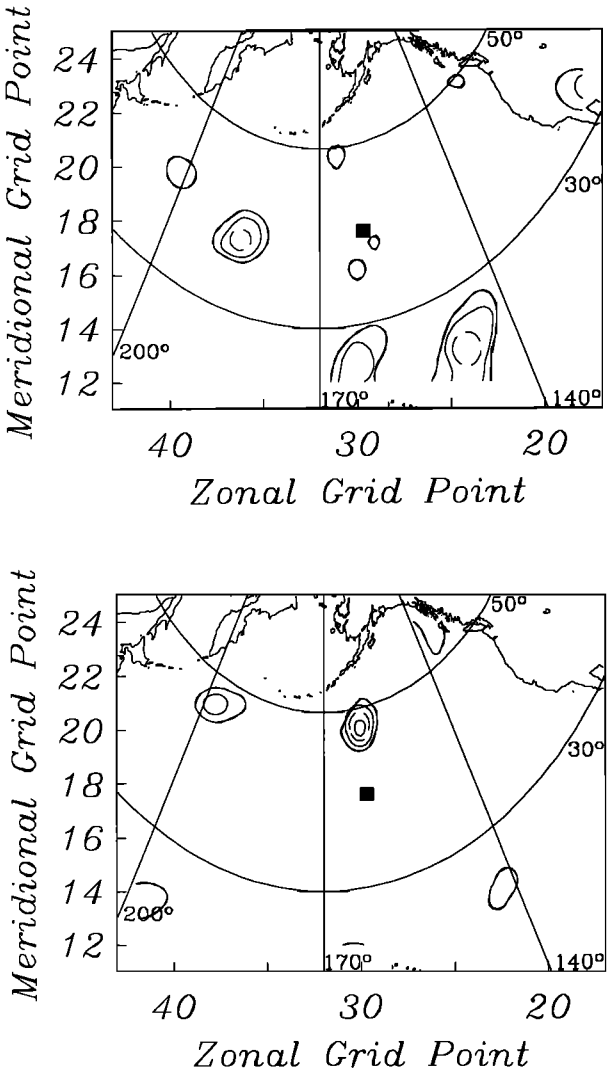

Fig. 16. Maps of the squared coherence between the (top) meridional and (bottom) zonal barotropic velocity at EJ and curl over the North Pacific for a period of 8.9 days. The location of EJ is shown as a solid square. Coherence contours are shown beginning at the zero coherence level at 95% significance of 0.31 (heavy line) and at intervals of 0.1 starting at 0.4, with odd contours shown as dashed and even contours as solid lines. The zonal velocity is forced from grid point 2030 to the north of the station with a peak coherence of 0.66 at a phase of ≈−150°, while the meridional velocity is forced from grid point 1736 located well to the west with a peak coherence of 0.52 at a phase of ≈20°.

site EJ as well; clockwise elliptic polarization is found at EI which is not seen at the remaining locations. For the 10-to-14-day band, clockwise polarization is apparent at EC and possibly EJ, while polarization appears counterclockwise at EB and EI with no preferred rotary polarization seen at the rest of the sites. There is no persuasive evidence for rotary polarization outside of these bands.

Finally, there is evidence for topographic effects in the spatial coherence patterns, especially at long periods. In the bands where common spatial patterns are observed, this usually takes the form of rotation of the symmetry axis in the general direction of the regional planetary vorticity contours (Figure 10). For some sensors, the pattern is shifted southward toward the observer, distorting the symmetry (Figure 11). The presence of substantial intersite differences suggests either local topographic effects or some additional, non-topographic mechanism.

6. WAVENUMBER SPECTRA

The availability of a coherent set of current sensors, such as the BEMPEX array, offers a rare opportunity to make direct estimates of the wavenumber structure of any propagating components. For a given period and velocity component, it is first necessary to select a subset of the sensors which are coherent. This is done by computing all possible two-point coherences and comparing the estimates at a selected period to the zero coherence level at 95% significance. If enough coherent sensors are found (typically, at least five), then a wavenumber estimator may be applied.

The expected spatial scales for propagating disturbances are those of mid-latitude barotropic Rossby waves, typically of the order of 1000 km or more. Since this is comparable to the size of the BEMPEX array, conventional wavenumber estimators will lack adequate resolution, hence wavenumber estimates were

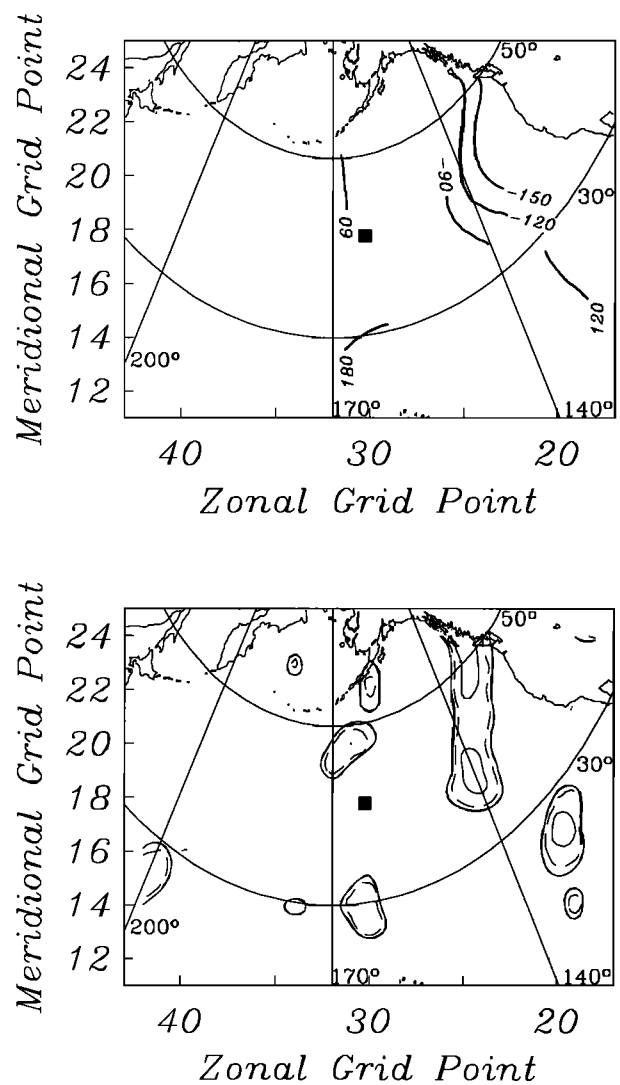

Fig. 17. Maps of the (top) phase and (bottom) squared coherence between the meridional barotropic velocity at EB and curl over the North Pacific for a period of 7.4 days. The location of EB is shown as a solid square. Coherence contours are shown beginning at the zero coherence level at 95% significance of 0.25 (heavy line) and at intervals of 0.1 starting at 0.3, with odd contours shown as dashed and even contours as solid lines. The inferred forcing location is in the vicinity of grid point 2325, where the coherence is 0.46. A positive phase means that curl leads the barotropic velocity.

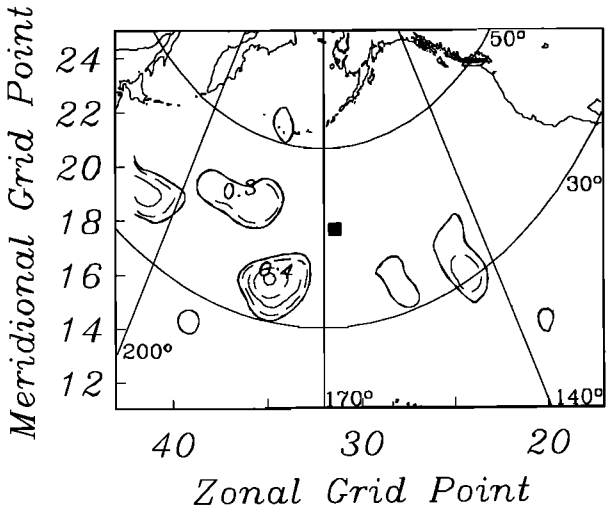

Fig. 18. Map of the squared coherence between the meridional barotropic velocity at EC and curl over the North Pacific for a period of 6.3 days. The location of EC is shown as a solid square. Coherence contours are shown beginning at the zero coherence level at 95% significance of 0.25 (heavy line) and at intervals of 0.1 starting at 0.3, with odd contours shown as dashed and even contours as solid lines. The inferred forcing location is at grid point 1635, where the coherence is 0.61 at a phase of ≈25°.

computed using the maximum likelihood method (MLM) of *Capon* [1969]. Unlike more conventional approaches, MLM employs a wavenumber spectral window whose shape and sidelobe structure is data-dependent and hence changes with the wavenumber in a well-defined, optimal manner. The resolution of MLM depends primarily on the incoherent noise present in the data and only weakly on the natural beam pattern of the array, making it ideal for sparse arrays. The numerical procedure is based on a straightforward combination of the multiple prolate window method for the frequency domain computations together with the MLM procedure for the wavenumber calculation. All estimates use the center periods and time-bandwidths listed in Table 3 to facilitate comparison to the coherence spectra from the previous section.

Capon and Goodman [1970] have shown that MLM spectra are χ^2 distributed with

$$\nu=2(m-k+1) \tag{5}$$

degrees of freedom, where m is the number of independent frequency domain estimates and k is the number of sensors. The wavenumber spectrum is ordinarily normalized by the peak value and plotted on a decibel (dB) scale, so that the statistic of interest is the variance of the logarithm of the ratio of two spectral estimates with equal degrees of freedom, which is just twice the variance of $\log s_\nu^2$. *Thomson and Chave* [1991] showed that $\mathrm{var}[\log s_\nu^2]=\psi'(\nu/2)$, where ψ' is the trigamma function. Formulas for the computation of ψ' are available in most mathematical handbooks. Thus, an approximation to the standard error on the wavenumber spectrum plotted in decibel is given by

$$\sigma_\nu = \frac{20}{\log 10}[\psi'(\nu/2)]^{1/2} \tag{6}$$

For six and twelve degrees of freedom, this yields ≈5.5 and ≈3.7 dB, respectively. While more rigorous, equation (6) yields an error estimate that is nearly identical to one derived directly from the definition of a confidence limit by *Chave et al.* [1991]. However, the biggest difficulty in applying (6) comes in correctly estimating the degrees of freedom ν; in particular, the sensors are unlikely to be independent, so (5) is an upper limit to the true value. To see this, imagine a noise-free plane wavefield such that, for the right choice of wavenumber, the signal at one sensor can be predicted from that at any other. In this instance, the degrees of freedom will be closer to $2m$. Since the true value is hard to estimate, it can only be bounded such that $2(m-k+1)\leq\nu\leq 2m$. For small values of m, this makes for a large uncertainty in both the variance and confidence limits derived from it. The situation is not satisfactory and could probably best be resolved by applying the nonparametric jackknife [*Thomson and Chave*, 1991], but such an effort is beyond the scope of this work.

Figure 21 shows the MLM wavenumber spectrum for the zonal barotropic velocity at a period of 13 days computed using five sensors. Comparable peak locations were obtained for other combinations of five sensors, although this particular

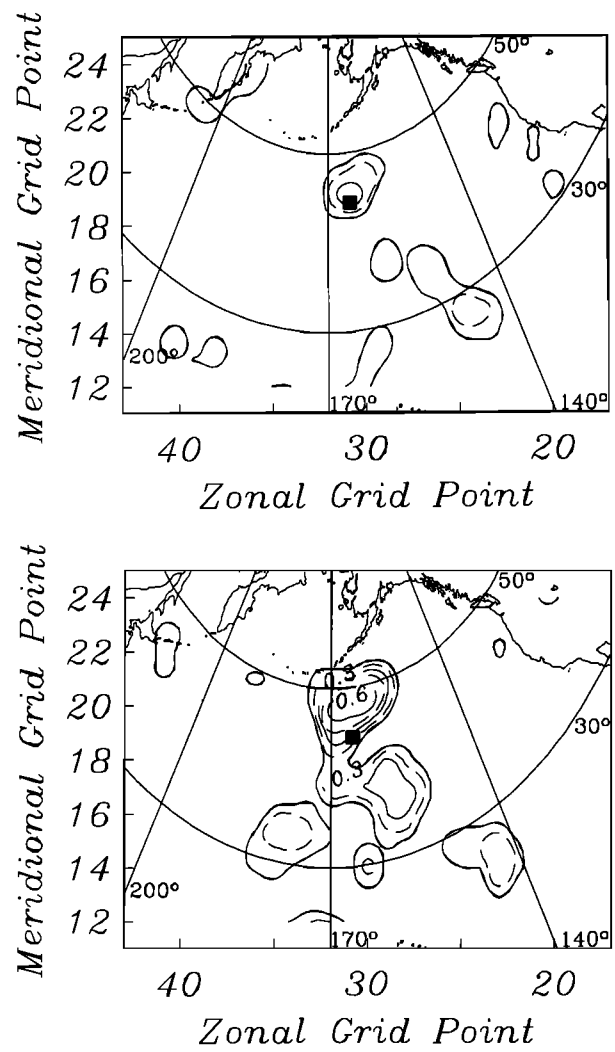

Fig. 19. Maps of the squared coherence between the (top) meridional and (bottom) zonal barotropic velocity at EE and curl over the North Pacific for a period of 5.4 days. The location of EE is shown as a solid square. Coherence contours are shown beginning at the zero coherence level at 95% significance of 0.22 (heavy line) and at intervals of 0.1 starting at 0.3, with odd contours shown as dashed and even contours as solid lines. Both velocity components exhibit local coherence, with the peak value displaced to the north for the zonal term. The zonal velocity peak coherence is 0.66 at a phase of ≈−90° (grid point 2031), while the meridional coherence is 0.46 at a phase of ≈90° (grid point 1931).

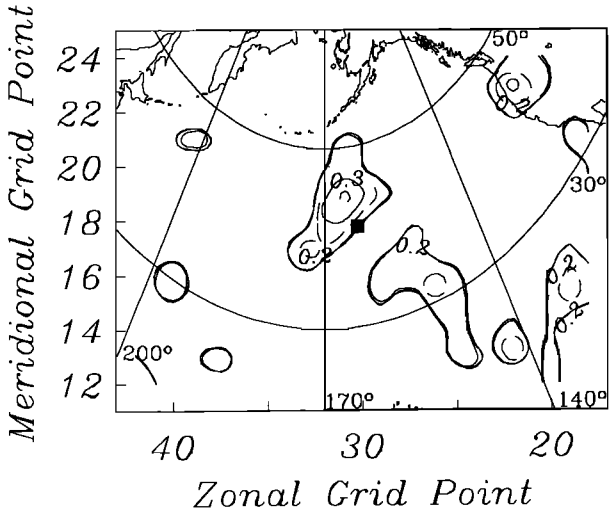

Fig. 20. Map of the squared coherence between the meridional barotropic velocity at EB and curl over the North Pacific for a period of 4.7 days. The location of EB is shown as a solid square. Coherence contours are shown beginning at the zero coherence level at 95% significance of 0.19 (heavy line) and at intervals of 0.1 starting at 0.2, with odd contours shown as dashed and even contours as solid lines. The inferred forcing location is at grid point 1931 where the coherence is 0.51 at a phase of ≈35°.

choice has the sharpest peak. However, if EB is included in the sensor suite, a shift to smaller meridional wavenumbers ensues and the estimate is degraded overall, probably owing to the strong rotary polarization at this site. Rotary polarization requires the presence of more than one significant wave component which could bias the MLM estimate. It is interesting to note that of the seven sensors, all but EM show the same strong north-northeast forcing point, yet inclusion of EM in the wavenumber estimate does not significantly alter the result. The wavelength inferred from the spectral peak is ≈3350 km.

Figure 21 also compares the resulting wavenumber estimate with Rossby wave dispersion or slowness circles computed for a flat-bottomed ocean and for one with linearly sloping topography with a non-zonal strike direction. The derivation for sloping topography and without the rigid lid approximation is a straightforward extension of a result from *Le Blond and Mysak* [1978, p. 184], yielding

$$k^2+\left[\frac{\beta}{\omega}-\frac{f\,\partial_\eta H}{\omega H}\cos\theta\right]k+l^2-\left[\frac{f\,\partial_\eta H}{\omega H}\sin\theta\right]l+\frac{f^2}{gH}=0 \quad (7)$$

where k,l are the east and north wavenumbers, θ is the positive counterclockwise topographic strike direction, and $\partial_\eta H$ is the gradient of topography. The orientation and magnitude of the bottom slope were derived from regional bathymetry for the North Pacific smoothed over a ≈100 km scale, yielding a 40° clockwise rotation from north for the slope direction and a fractional slope ($\partial_\eta H/H$) of ≈-0.15 Mm^{-1}. For these parameters, topography enhances the planetary vorticity gradient, resulting in an increase in the dispersion circle radius over that for a flat-bottom; the cutoff period is reduced to 2.0 days from the flat-bottomed value of 3.5 days. In addition, the circle is rotated according to the effective β. The fit of the sloping bottom slowness circle is qualitatively better than for the flat bottom case, and suggests that simple linear Rossby wave propagation modified by large scale topography is consistent with the BEMPEX velocity data.

Figure 22 compares zonal barotropic velocity wavenumber spectra at all periods where sufficient numbers of coherent sensors were available to produce a reliable result. Figure 23 shows a similar set of meridional velocity spectra but for different periods. Table 4 lists the sensors used, peak wavenumbers, and inferred wavelengths. The consistency of the peaks with the dispersion relationships is better than the error estimate (equation (6)) would suggest. As for Figure 21, the result is not overly sensitive to the specific sensor subset used in the estimate. There are a number of interesting trends in Figures 22–23 and Table 4 that should be noted. First, the zonal velocity phase propagation direction is consistently in the north-northwest direction while the shorter-period, meridional velocity propagates to the west-northwest. The group velocities are in the direction of the centers of the slowness circles, hence

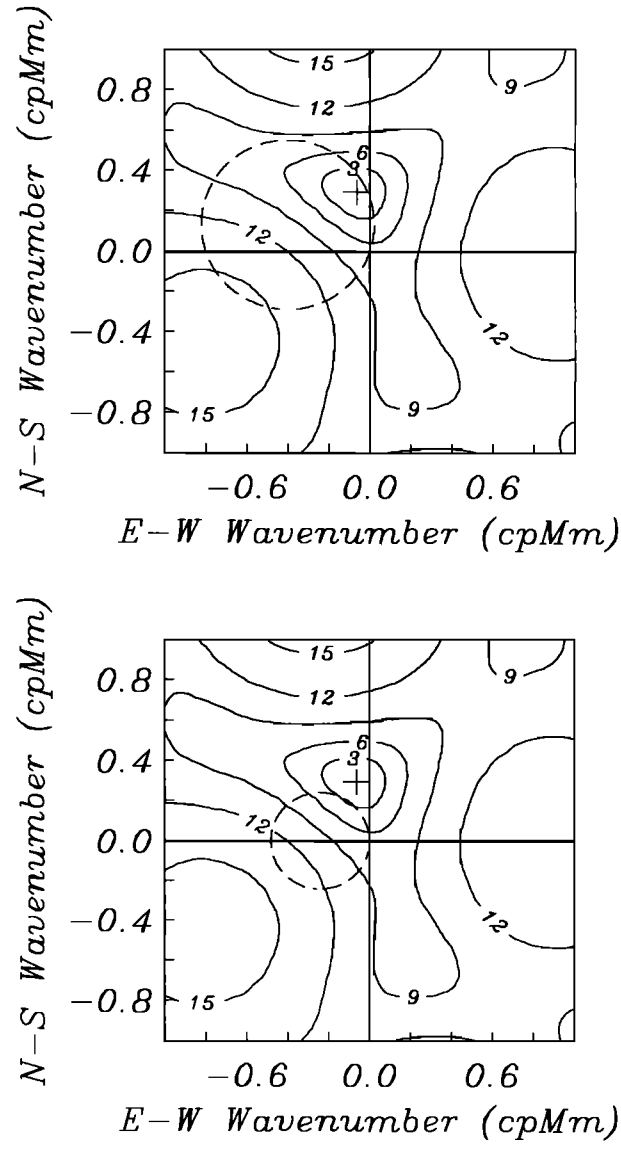

Fig. 21. Wavenumber spectra for the zonal barotropic velocity at 13 days computed using EE, EI, EC, EL, and EM. The spectrum peak is denoted by a cross, and the contours are shown in decibels down from that value. The dashed line in the bottom panel is the dispersion circle for a 13-day flat-bottom Rossby wave at 42°N, while the dashed line in the top panel shows the corresponding dispersion circle for a 13-day Rossby wave in the presence of linearly sloping topography as discussed in the text. The wavenumber spectrum has 6 to 14 degrees of freedom, yielding a standard error of 3.4 to 5.5 dB.

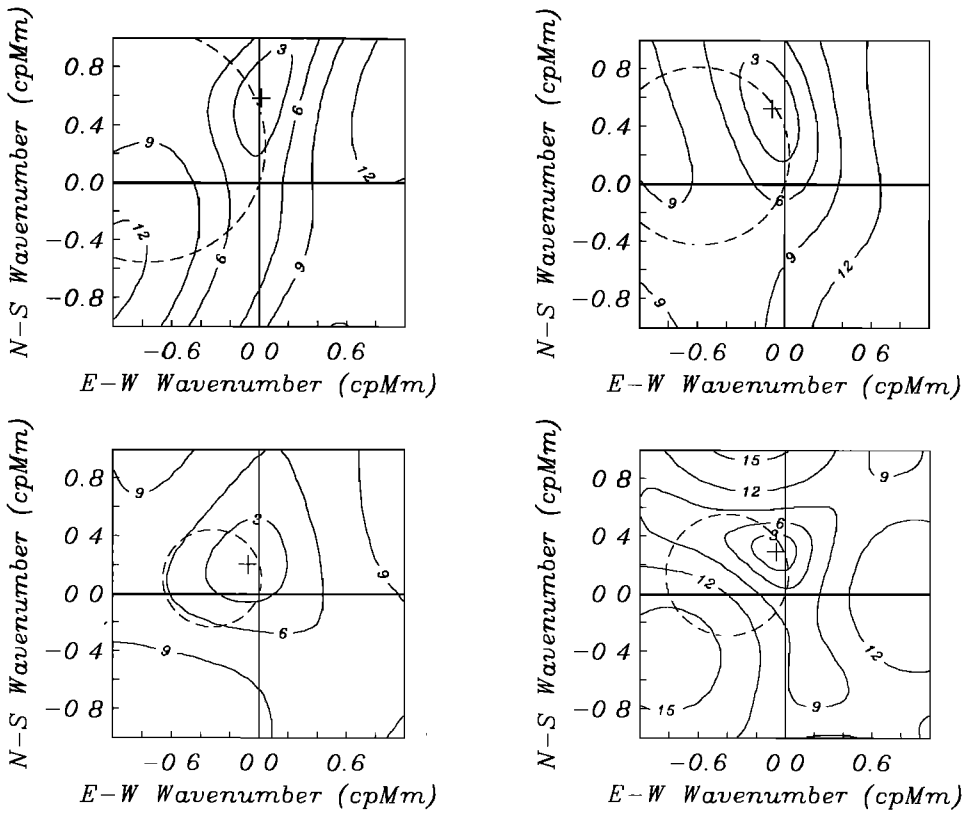

Fig. 22. Wavenumber spectra for the zonal barotropic velocity at periods of (clockwise from top left) 25, 19, 13, and 10 days computed using the sensors listed in Table 4. The spectrum peak is denoted by a cross, and the contours are shown in decibels down from that value. The dashed lines are slowness circles for Rossby waves at the appropriate periods in the presence of linearly sloping topography, as discussed in the text. The spectra have 6 to 14 degrees of freedom, yielding a standard error of 3.4 to 5.5 dB.

to the west-southwest for the zonal component but to the east-southeast for the meridional terms. Second, for those periods where wavenumber estimates may reliably be computed, the zonal velocity spectral peaks occur at large meridional wavenumbers, while the meridional velocity spectral peaks occur at large zonal wavenumbers. Third, the wavelength for the zonal velocity approaches basin scale as the period decreases, with a ≈5000 km wavelength being reached at about 10 days. Finally, there is a weak suggestion in Figure 23 that the meridional velocity wavenumber approaches the zonal axis, then moves toward larger scales until the cutoff value is reached. This is masked by a rising relative noise level below 6 days.

7. Discussion

Comparison With Current Meter Coherences

The most striking differences between the present observations and those of *Brink* [1989] and *Samelson* [1990] are the consistently higher BEMPEX coherences. This holds both for the absolute magnitude and with respect to the level of zero significance. The importance of choosing the narrowest spectral bandwidth possible commensurate with adequate statistical precision has been emphasized in section 5, and it was further suggested that the much lower coherences between currents and curl observed by Brink and Samelson might be due in part to the larger bandwidths of their analysis products.

However, there is another possible contributor. Both Brink and Samelson used data from single current meters rather than a barotropic product derived from an entire mooring, and it is possible that baroclinic contamination of the velocity data bears partial responsibility for the reduced coherence. To test this hypothesis, coherence maps were computed using the time-bandwidths of Table 3 for the zonal velocity measured by three vector-measuring current meters at 176, 943, and 2498 m on the central BEMPEX mooring located ≈6 km from site EB. The mooring details are given by *Luther et al.* [1991].

For the long-period group (68-to-19-day bands), the coherence patterns for the electrometer and the two deepest current meters are very similar. The coherence is comparable to, or slightly higher for, the electrometer, while the two deeper current meters give nearly identical results. The shallow current meter displays weaker coherence overall with a concomitant shrinking of the significantly coherent area. However, beginning at 13 days, the current meters consistently deliver weaker coherences as compared with the electrometer. Figure 24 shows the 2498- and 943-m results for 13 days which should be compared with Figure 14; the 176-m instrument gives only slightly better results than the 943-m unit. The double-lobe pattern which is clearly seen in Figure 14 is present but weaker for the 2498-m measurement, being especially small at the southeast peak, and is almost unrecognizable at 943 m. The zero crossing for the dynamic first baroclinic mode is located at ≈1800 m, and the amplitude is stronger at 943 than at 2498 m, as are the next few linear dynamic modes, suggesting that stronger baroclinic effects will be seen at 943 m. Furthermore, empirical orthogonal function (EOF) analysis of the mooring data suggests a first mode that appears to be barotropic but with moderate

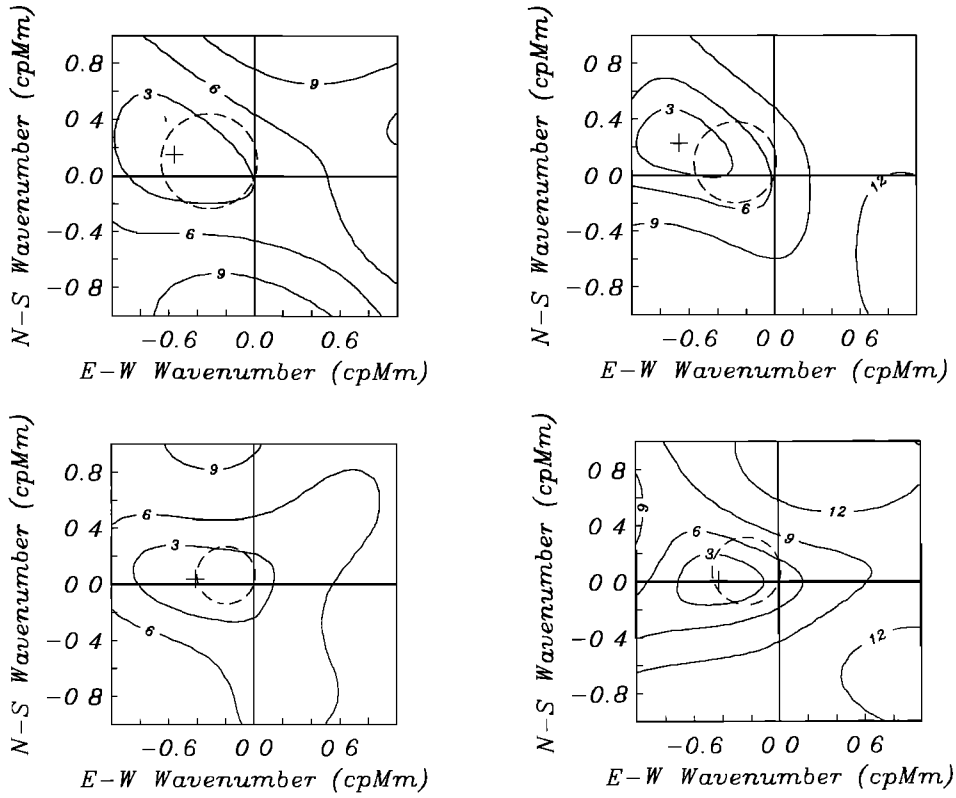

Fig. 23. Wavenumber spectra for the meridional barotropic velocity at periods of (clockwise from top left) 10, 8.9, 7.4, and 6.3 days computed using the sensors listed in Table 4. The spectrum peak is denoted by a cross, and the contours are shown in decibels down from that value. The dashed lines are slowness circles for Rossby waves at the appropriate periods in the presence of linearly sloping topography, as discussed in the text. The first two spectra have 8 to 16 degrees of freedom, yielding a standard error of 3.2 to 4.6 dB. The second two spectra have 12 to 22 degrees of freedom, yielding a standard error of 2.7 to 3.7 dB.

intensification above 500 m depth and a second empirical mode that is similar to the dynamic first baroclinic mode. The former accounts for up to 80% of the variance at periods over 15 days, dropping below 40% for periods shorter than 10 days. These observations are qualitatively consistent with the decrease in current meter-to-curl coherence at short periods as well as the similarity of the longer-period current meter and electrometer results. They also underscore the importance of using a measurement technology or analysis methodology which filters out the baroclinic component when looking for forced barotropic oscillations; based on mooring EOF analysis, the first baroclinic-like second mode accounts for only one-third as much variance as is explained by the nearly barotropic first mode at 13 days, yet the reduction of coherence in Figure 24 as compared with Figure 14 is substantial. Thus, it appears that both analysis bandwidth and lack of baroclinic contamination are important in explaining the markedly higher velocity-to-curl coherences obtained during BEMPEX.

Comparison With Model Predictions

Treguier and Hua [1987] have attempted to model atmospherically induced fluctuations using a flat-bottomed, nonlinear, stratified quasi-geostrophic model which is forced by stochastic curl. Their results indicate a nearly linear barotropic response at scales larger than ≈500 km where resonant Rossby wave excitation is balanced by bottom friction, whereas the baroclinic response typically involves nonlinear processes. Thus, for the spatial scales and period ranges studied in BEMPEX, as reflected in Tables 3 and 4, it appears that linear ocean behavior is expected, and it is appropriate to contrast the observations with simple linear models.

The coherence in the BEMPEX data is dominantly nonlocal, hence the most useful comparisons are to the models of *Brink* [1989], *Samelson* [1989], and *Samelson and Shrayer* [1991]. It should be remembered that various parameters in the cited models, notably the frictional damping, have been adjusted to

TABLE 4. Peak Wavenumber Estimates

Component	Period	Sensors	k_x,cpMm	k_y,cpMm	Wavelength, km
Zonal	25	ECBJM	0.0128	0.5897	1700
Zonal	19	ICBJM	-0.0897	0.5256	1880
Zonal	13	EICLM	-0.0641	0.2949	3350
Zonal	10	ECBJLM	-0.0769	0.2051	4570
Meridional	10	EICBL	-0.5641	0.1538	1710
Meridional	8.9	EICBJL	-0.6667	0.2308	1420
Meridional	7.4	ICBJLM	-0.4231	0.0128	2360
Meridional	6.3	EICBM	-0.4103	0.0385	2430

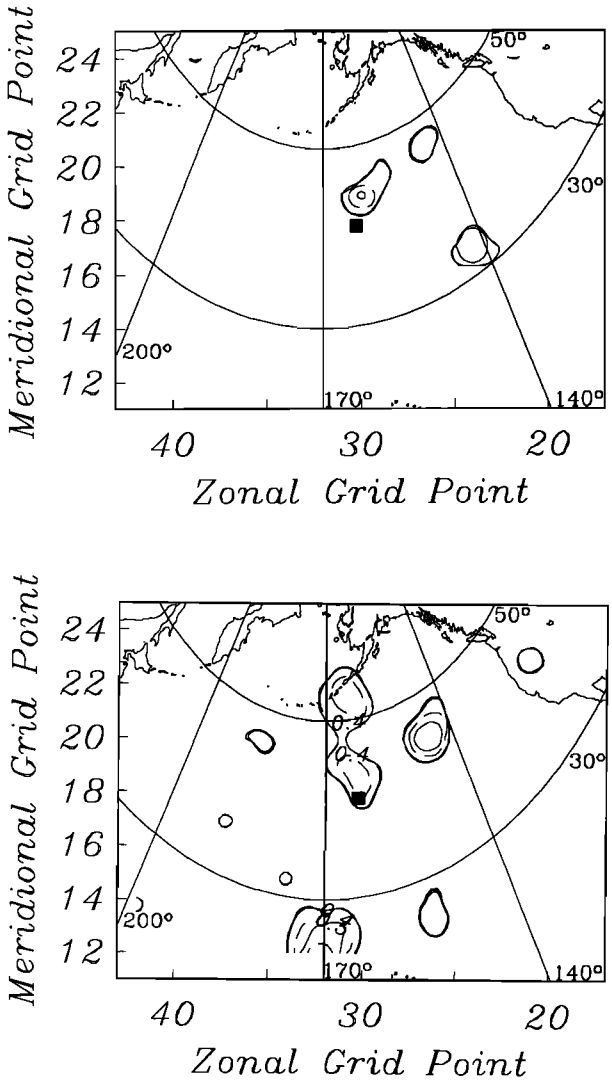

Fig. 24. Squared coherence maps with curl for the zonal velocity from vector measuring current meters at (top) 943 m and (bottom) 2498 m on a subsurface mooring located near EB at a period of 13 days. The mooring location is shown by the solid square. Coherence contours are shown beginning at the zero coherence level at 95% significance of 0.39 (heavy line) and at intervals of 0.1 starting at 0.4, with odd contours shown as dashed and even contours as solid lines. The peak coherence for the 943-m sensor is 0.62 at grid point 1930, while it is 0.67 at grid point 2026 for the 2498-m instrument.

agree with the lower coherences observed in their field studies. It is possible that friction in the real ocean is larger than is reflected in the models; an increase in friction is expected to result in more damping of free Rossby waves, a concomitant decrease in the wavenumber bandwidth, and hence an increase in the barotropic velocity-to-curl coherence. However, both Brink and Samelson indicate that their models are not overly sensitive to the strength of friction. It is also possible that the curl parameterization used by them underrepresents the real forcing. Note that a factor of 2 decrease in the e-folding scale of the autocorrelation of curl between *Samelson* [1990] and *Samelson* [1992] led to roughly a doubling of the velocity-to-curl coherence, indicating that the model is quite sensitive to the forcing correlation scale. However, even the higher coherences in the Samelson and Shrayer model fail to reach those which are observed in the BEMPEX data. The presence of multiple peaks in the curl autocorrelation function, which is observed for real curl [*Chave et al.*, 1991] but is absent from the models, will also increase the excitation. Thus, inadequate curl parameterization may explain part of the discrepancy. Finally, Samelson's model also contains a meridional barrier to represent the Mid-Atlantic Ridge which acts to increase the velocity-to-curl coherence to its east through Rossby wave reflection. A comparable feature does not exist in the BEMPEX area, although the narrow Emperor Seamount chain may have a similar effect. Thus, quantitative comparisons of the modeled and observed coherence magnitudes should await model runs with geometries more suitable for the North Pacific and will not be pursued further.

The coherence phase may be less sensitive to details of the forcing and hence may be more suitable for comparison purposes. An interesting trend appears in the coherence phase in Figures 10 and 13–14. Note that the phase convention used here is opposite to that used by *Brink* [1989], *Samelson* [1989, 1990], and *Müller and Frankignoul* [1981]; in the following, their results will be reversed in sign. At the longest period of 38 days seen in Figure 10, the zonal double-lobe displays a northeastern phase of ≈0° and a southeastern phase of ≈180°. Similar values are seen at the remaining sites which have a zonal double-lobe pattern, although at EB (where there is strong rotary polarization), the northeastern value is closer to 30° and the southeastern one is ≈160°. At 25 days period, the northeastern and southeastern phases are consistently 30°–40° and 180° at all coherent sites. At 13 days (Figures 13–14), the northeastern phase is 110°–120° except at EB, where it drops to ≈90°. At 10 days, the phase at the northeast lobe increases sharply to 270°, while at 8.9 days it is ≈–150°. Thus, there appears to be a strong increase in phase with period at the northeast lobe. There is some suggestion for this between the 49-day model of *Brink* [1989] and the 5-day computation in *Samelson* [1990], where the phase ranges from ≈130° to ≈–90° at the northeast lobe and ≈40° to ≈90° at the southeast lobe. Thus, the models at least indicate a phase change with frequency, and it is possible that adjustment of a North Pacific version of the models to match the observed phase change would provide further insight into atmospheric forcing. However, the 38-day local coherence for EC (meridional) in Figure 10 is ≈65°, which is in conflict both with Brink's 49-day value of ≈–60° and the 0° expected for a Sverdrup balance. Furthermore, the observed phases at the two nonlocal zonal peaks do not agree with the model values.

The major similarities between this study and the nonlocal forcing models are qualitative rather than quantitative. The existence of a zonal double-lobe is a reasonably robust feature of the 38-to-25-day data, and this may actually be a single northeastern lobe, as seen at 13 days and predicted by *Samelson and Shrayer* [1991] when a northward increase in curl power is included in the model. The northern lobe appears to move closer to the station until it lies directly to the north at 8.9 days, another model feature. However, a meridional Sverdrup balance is not commonly observed.

There remain a number of significant differences between observation and model. There is increasing evidence for the forcing location to be nonlocal and west of the site at periods shorter than 10 days, yet this is only weakly evident in the models. More prominently, there is substantial variability in the azimuth and distance of the coherence patterns between stations at a given period and between periods for a given station. It is rare for even the majority of stations to show identical coherence behavior at a given period. This probably reflects some

combination of the spatial variability of curl, the influence of topography, and spatially varying noise levels. Topographic effects are suggested by the clockwise rotation of the double lobe pattern at 38 and 25 days to align with the regional planetary vorticity contours shown in Figure 2. However, there is intersite scatter in the rotation angle which might reflect local topography.

There are other phenomena in the data which are probably caused by the variability of curl in space and with period which are not contained in the models. First, at some periods there is a single, persistent hot spot which serves as the forcing location for a number of stations at a number of periods; examples occur at 38, 25, and 13 days. Second, there are many instances where more than one forcing location is implicated. This is especially prevalent at periods under 10 days. Third, stronger patterns are observed in certain period bands which coincide with enhanced power in the data. Finally, strong rotary motion is occasionally observed. This requires two phase-locked waves which might be produced by phase-locked forcing at multiple locations, suggesting persistent atmospheric teleconnections over long ranges. Further evidence for the importance of curl variability will be presented at the end of this paper.

Müller and Frankignoul [1981] provide predictions of the local coherence between barotropic velocity and the atmospheric variables to which quantitative comparison can be made when local coherence exists, expanding on some preliminary remarks given by *Luther et al.* [1990]. A major discrepancy between model and observation is immediately evident: significant local barotropic velocity-to-curl coherence is predicted only at periods in excess of 100 days, yet occasional local coherence is observed at shorter periods. There is some agreement between the predicted phase and the observations; Müller and Frankignoul give a ≈90° phase at 40-days period, which is not far from the observed 65° in Figure 10. However, the observed and model phases do not agree for the topographic Sverdrup balance seen at EL for 38 days, where the phase is ≈-140°. It is possible that much of the local coherence observed in the BEMPEX data is topographically controlled, making comparisons with flat-bottomed model results fruitless.

Müller and Frankignoul also predict significant local coherence of zonal (meridional) velocity with zonal (meridional) wind stress and very weak coherence of meridional velocity with air pressure at short (below Rossby wave cutoff) periods. Lack of local coherence with these atmospheric variables at long periods is a surprisingly robust feature of the data. In those unusual instances where statistically significant local coherence is seen, it is invariably at the edge of a large nonlocal patch. At shorter periods, local coherence is more common, although not ubiquitous, but is frequently observed in the wrong velocity components, suggestive of topographic effects. While the BEMPEX velocity data are not coherent with the atmospheric variables below the Rossby wave cutoff due to ionospheric noise, some coherence comparisons in its vicinity are provided in Figures 25–27 for, respectively, EM (meridional) with air pressure at 7.4 days, EB (meridional) with meridional wind stress at 5.4 days, and EE (zonal) with zonal wind stress at 5.4 days. Müller and Frankignoul predict an in-phase local coherence for meridional velocity with air pressure of ≈0.15 at periods below the barotropic Rossby wave cutoff. Figure 25 is for a somewhat longer period, and the observed -140° phase is in rough agreement with the model. However, the observed local coherence of ≈0.5 is far in excess of the model prediction. Unfortunately, verification of the model trend to zero phase at shorter periods

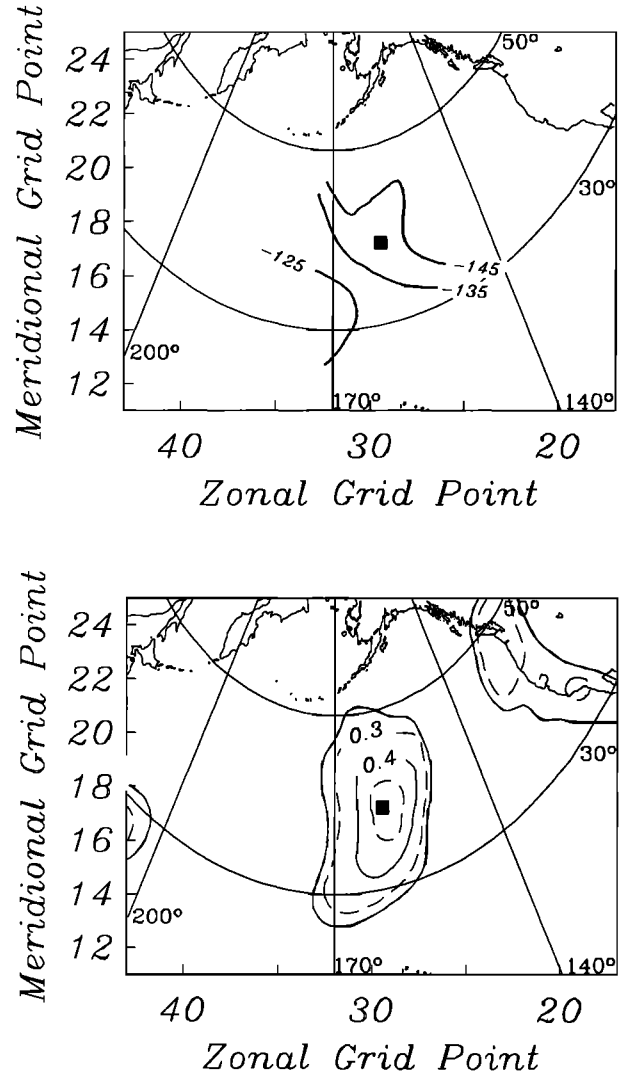

Fig. 25. Maps of the (top) phase and (bottom) squared coherence between the meridional barotropic velocity at EM and air pressure over the North Pacific for a period of 7.4 days. The location of EM is shown as a solid square. Coherence contours are shown beginning at the zero coherence level at 95% significance of 0.25 (heavy line) and at intervals of 0.1 starting at 0.3, with odd contours shown as dashed and even contours as solid lines. A positive phase means that air pressure leads the barotropic velocity.

is precluded by weak coherence. Müller and Frankignoul also predict strong local coherence of ≈0.6 for barotropic currents with wind stress for periods below the barotropic Rossby wave cutoff. Figures 26–27 are for slightly longer periods yet show strong local coherence approaching the model value. The observed phase of 90° is in good agreement with the model prediction below cutoff. Thus, there appears to be better consistency of the wind stress than the air pressure coherences with the Müller and Frankignoul model.

Finally, *Cummins* [1991] concluded on the basis of numerical modeling that the vorticity balance at a point is wave-like in the North Pacific at periods under 100 days, as is observed in the BEMPEX velocity data. He further asserted that a topographic Sverdrup balance emerges when large-scale averages of the vorticity terms are taken. As a simple test of this hypothesis, point-by-point averages of the time series were obtained and maps between the composite data set and the atmospheric vari-

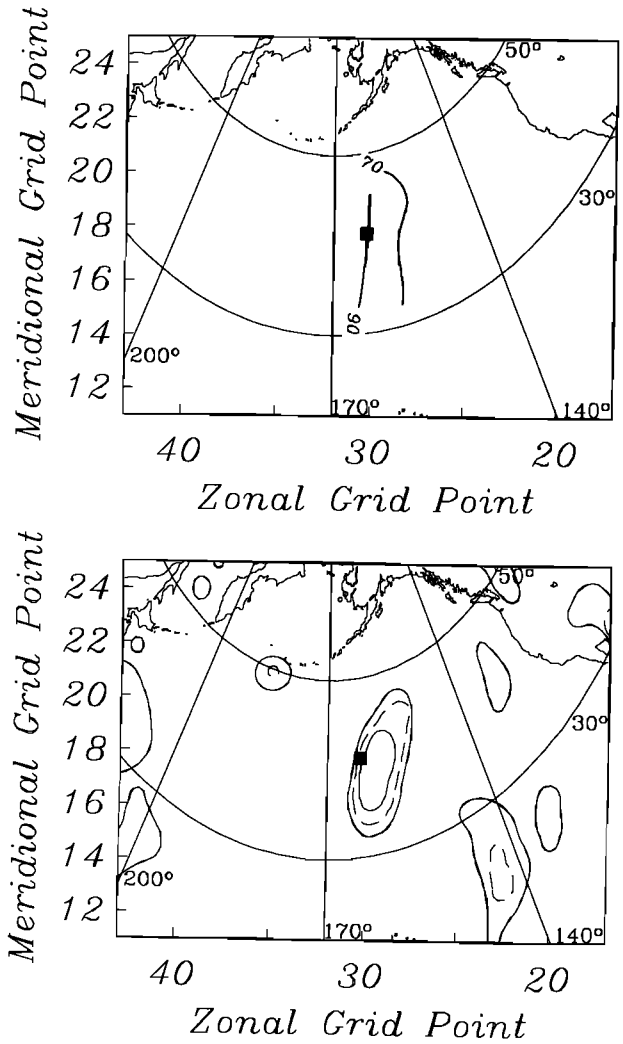

Fig. 26. Maps of the (top) phase and (bottom) squared coherence between the meridional barotropic velocity at EB and the meridional wind stress over the North Pacific for a period of 5.4 days. The location of EB is shown as a solid square. Coherence contours are shown beginning at the zero coherence level at 95% significance of 0.22 (heavy line) and at intervals of 0.1 starting at 0.3, with odd contours shown as dashed and even contours as solid lines. A positive phase means that wind stress leads the barotropic velocity.

ables were computed. The result shows a strong local coherence of the meridional velocity with curl; the average of EB, EC, EJ, EL, and EM shows a Sverdrup balance at all periods longer than 15 days. Further details will be reported elsewhere.

Spatial Coherences and Wavenumber Estimates

The preponderant observation in section 6 is the tendency for westward zonal and eastward meridional group propagation at periods longer or shorter than ≈10 days, respectively. At least for the long period, zonal velocity, this is in good agreement with the inferred forcing locations, but there are some discrepancies for the meridional terms, especially at 7.4 days. It is instructive to examine the relation between atmospheric forcing and group propagation in more detail. However, it should be remembered that different questions are being addressed with the coherence maps and wavenumber spectra, and any connection between the two is an assumption rather than a requirement.

For the zonal component, the most persistent coherence patterns and largest coherences occur at 25 and 13 days. The computed wavenumbers at these periods (Figure 22 and Table 4) are in the north and north-northeast directions, respectively, so that the inferred group propagation is to the west-southwest and southwest. Both of these directions are consistent with forcing locations which reconcile the various coherence maps at most of the sites. Note that the double-lobe coherence pattern at 25 days could not be explained solely by either the northeast or southeast patches due to strong complementary curl intercorrelation between these locations. The wavenumber spectra suggest that it is the northeast lobe which is dominantly responsible for the forcing, a conclusion which is supported by the *Samelson and Shrayer* [1991] model, which incorporates a realistic northward increase in curl power, and by the 13-day observations. As a cautionary note, two of the sites used to get the 25-day wavenumber spectra are rotary polarized (EB and EJ), requiring a second phase-locked wave to be present and possibly biasing

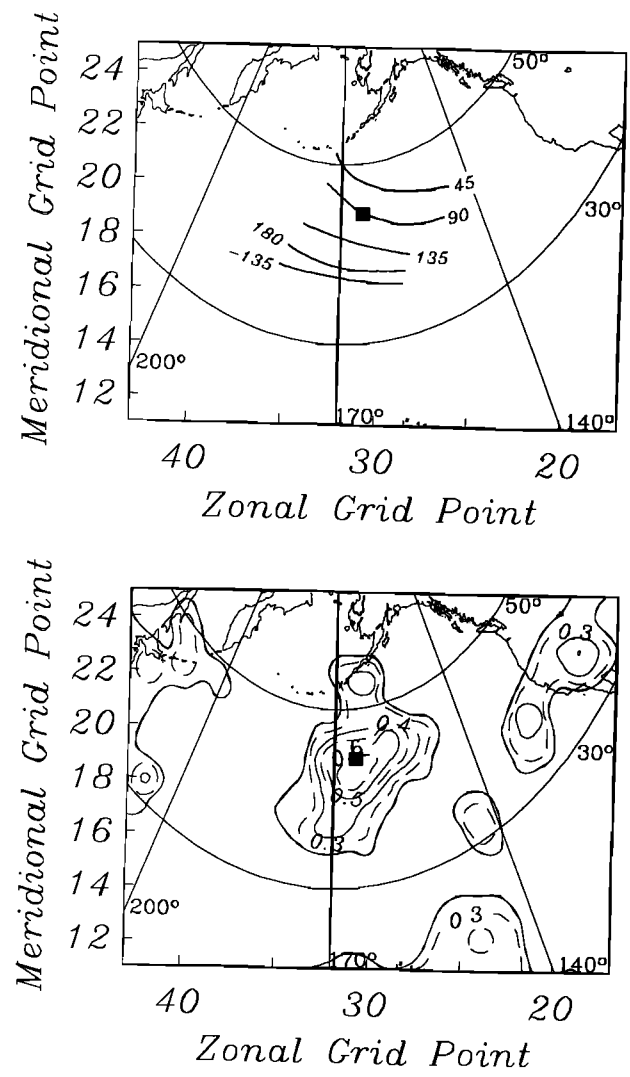

Fig. 27. Maps of the (top) phase and (bottom) squared coherence between the zonal barotropic velocity at EE and the zonal wind stress over the North Pacific for a period of 5.4 days. The location of EE is shown as a solid square. Coherence contours are shown beginning at the zero coherence level at 95% significance of 0.22 (heavy line) and at intervals of 0.1 starting at 0.3, with odd contours shown as dashed and even contours as solid lines. A positive phase means that wind stress leads the barotropic velocity.

the MLM estimate as it clearly did at 13 days (see section 6). However, the consistency of the zonal wavenumber results in Table 4 argues against any strong bias effects at 25 days. The remaining zonal wavenumber spectra are somewhat more difficult to explain. The predominant forcing point at 19 days is located to the east-southeast which is marginally feasible given the large uncertainty region in Figure 22. However, the similarity of the peak wavenumbers at 25 and 19 days (Table 4), the strength of the 20-to-50-day peak at many sites, and the ≈50% overlap between adjacent bands (Table 3) suggests that the 19-day estimate is simply weighted toward the lower-frequency result. At 10 days, the uncertainty region encompasses much of the Rossby wave slowness circle, reflecting the presence of multiple sources, an increase in the wavenumber bandwidth, and a concomitant reduction in coherence. This makes any meaningful conclusions difficult to draw.

More variability in forcing location was encountered at periods under 10 days, excepting 7.4 days, and this is reflected in the larger confidence regions in Figure 23 as compared with Figure 22. In fact, it is only at 8.9 and 7.4 days that eastward group propagation can be inferred with any degree of certainty. At both 10 and 6.3 days, the confidence region encompasses most of the slowness circle, probably reflecting the combination of southwest, south, and eastern forcing points required to explain the velocity-to-curl coherences and suggesting that multiple free waves are present. At 8.9 days, the group propagation is clearly to the east-southeast, reflecting the occurrence of forcing points west of the BEMPEX area in this band. The 7.4-day band is something of an anomaly since the forcing appears unambiguously to be from the east, yet group propagation is clearly eastward. This presents something of a paradox, but there are at least three possible ways to reconcile these two observations.

First, the wavenumber spectra may be dominated by a propagating component from a western source which is not of atmospheric origin, such as an instability of the Kuroshio. The MLM algorithm will tend to isolate the dominant wavenumber component at a given frequency and hence might eliminate the effect of a wind-forced, westward-propagating disturbance. This scenario cannot be ruled out, but it also cannot be tested with the present data.

Second, a multiplicity of wavenumbers might be present such that the MLM estimator picks out those with an eastward group velocity even though an eastern forcing point is the strongest and most consistent location in the curl maps. This situation is difficult to accept for a variety of reasons. The results for EI presented in Figures 7–9 clearly show that the forcing region with the strongest correlation, which is located off of North America, is consistent with the curl, wind stress, and air pressure coherences. In particular, the weaker curl coherence located west of the station is a much poorer fit, especially for the air pressure maps in Figure 9. Of the remaining sites, only EC shows any significant western coherence with curl, and this location is not a forcing point based on curl intercorrelation analysis. The remaining stations more closely resemble Figure 17 and show no evidence of western driving. Unless the concept of stealth forcing from the west is acceptable, it is difficult to see how any significant eastward group-propagating component of atmospheric origin could be present in the 7.4 day band.

Finally, it is possible that long Rossby waves are excited at the strong coherent patch in the eastern North Pacific, group propagate to the west, reflect off of a topographic barrier as short Rossby waves, and are detected at the BEMPEX array. A candidate reflector is the Emperor Seamount chain located ≈2000 km to the west of the BEMPEX array. This is an irregular feature which rises almost continuously to within 1000 m of the sea surface with individual elements that are much shallower. It is much harder to envisage reflection from the western edge of the basin given its remoteness and irregularity. Given the reflection properties of Rossby waves [*Longuet-Higgins*, 1964], the nearly zonal phase and east-southeast group velocities inferred from Figure 23 are consistent with normal reflection from the Emperor chain of a nearly zonal long wave having a westward group velocity. It is easy to see why the MLM estimator would pick out the short-wavelength, reflected wave in meridional velocity and ignore the incident, large-wavelength component since the latter would be expected to have a weaker meridional velocity signature. Pressure data would be more sensitive to a long-wavelength component, and it is interesting to note that a wavenumber spectrum of the BEMPEX pressure data at 7.4 days shows a northward phase- and westward group-propagating component at about the right place to be the incident wave. However, it is not obvious that a feature like the

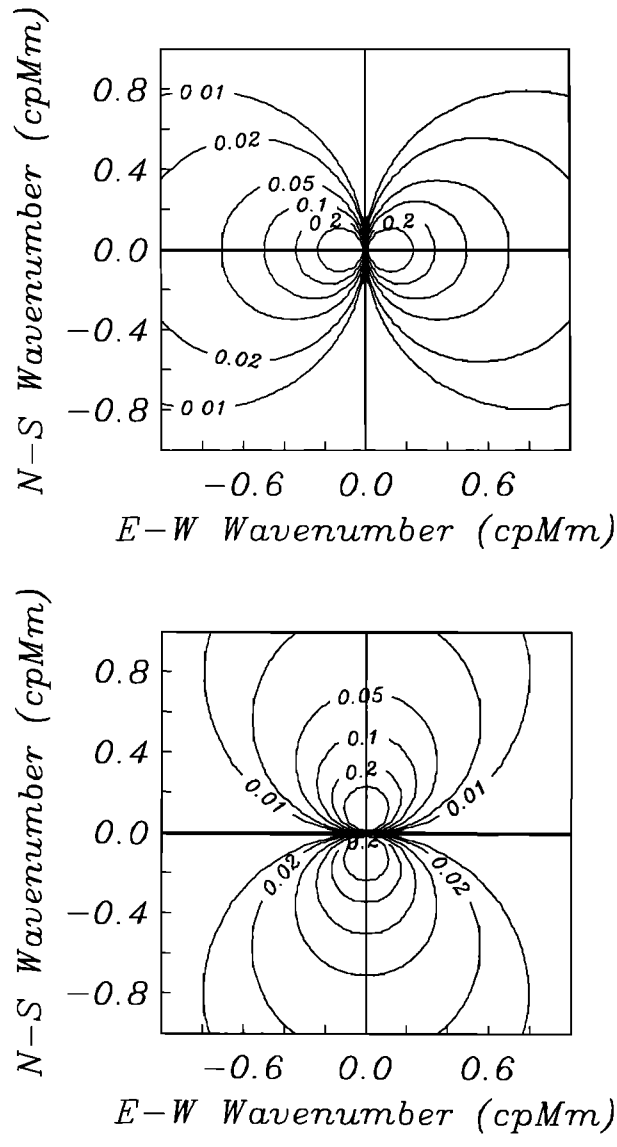

Fig. 28. Contours of the absolute square of equation (9) for the (top) meridional and (bottom) zonal barotropic velocities.

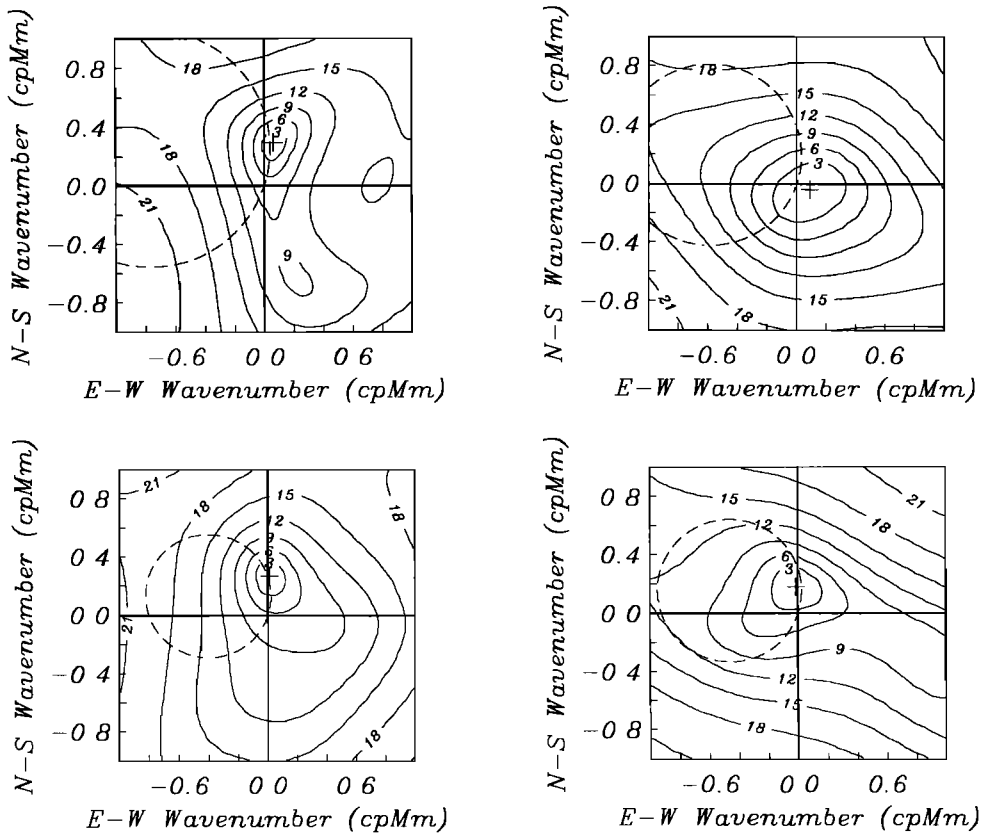

Fig. 29. Wavenumber spectra for curl at grid point 2027 for periods of (clockwise from top left) 25, 19, 15, and 13 days. The spectral peak is denoted by a cross, and the contours are in decibels down from the peak. The spectra have 6 to 14 degrees of freedom, yielding a standard error of 3.4 to 5.5 dB. The peak power is, respectively, 1.65, 0.87, 0.84, and 1.20 $\times 10^{-15}$ dyn^2 cm^{-6} cpd^{-1} at the four periods.

Emperor chain is a strong reflector for Rossby waves. *Rhines* [1969] derives an expression for the transmission coefficient of a two-dimensional ridge, and with parameters suitable for normal incidence on the Emperor Seamounts, the corresponding reflection coefficient is extremely small. However, the seamount chain is only about one wavelength long, so the infinite length approximation is not valid. Given the irregularity of the Emperor chain, a numerical simulation is probably the best way to further investigate these observations.

Final Remarks

The *Müller and Frankignoul* [1981] model is especially useful for demonstrating the consistency of major features of the BEMPEX data with simple, linear, atmospheric forcing dynamics. In particular, they give frequency-wavenumber domain expressions for the transfer functions $T(\vec{k},\omega)$ relating a given atmospheric variable $X(\vec{k},\omega)$ to an oceanic variable $Y(\vec{k},\omega)$. It is worth pointing out that these expressions could easily be adapted to compute nonlocal coherence, although this was not done by them. Using the transfer functions, it is simple to relate the frequency-wavenumber spectrum of the barotropic velocity to that of curl. The relevant expression for T taken from Muller and Frankignoul's Table 1 is

$$T(\vec{k},\omega) = K(\vec{k})\Omega(\omega) \tag{8}$$

where

$$K(\vec{k}) = -\frac{\varepsilon_{ij}k_j}{k^2+R_o^{-2}} \tag{9}$$

and ε_{ij} is the permutation tensor, while R_o is the barotropic Rossby radius of deformation. The frequency dependence Ω is given by

$$\Omega(\omega) = \frac{1}{\omega-\omega_o+iD} \tag{10}$$

where ω_o is an allowed barotropic Rossby wave frequency from the dispersion relation and D is a dissipation parameter. Equation (10) is effectively a resonance at the Rossby wave frequency damped by friction, hence will display small peak frequency shifts and a broader width as friction increases.

Figure 28 shows the absolute square of (9) for the zonal and meridional velocities, from which it is clear that the zonal (meridional) velocity is preferentially sensitive to curl power in the vicinity of the meridional (zonal) wavenumber axis, peaking at a meridional (zonal) wavenumber of R_o^{-1}. In the presence of sloping topography, the patterns in Figure 28 are rotated according to the effective β; this is a clockwise rotation of $\approx 20°$ from Figures 21–23 for the BEMPEX region.

Figure 28 can be used to reconcile Figures 22–23, where the zonal (meridional) velocity observations contain dominant components along the meridional (zonal) wavenumber axes. The velocity wavenumber spectrum is controlled by three quantities, namely (9), the frequency dependence (10), which is largest at a given frequency for points near the Rossby wave slowness circle, and the frequency-wavenumber spectrum of curl at the forcing point. Thus, the strongest velocity wavenumber spectrum will occur for points where (9) is large and the curl forcing

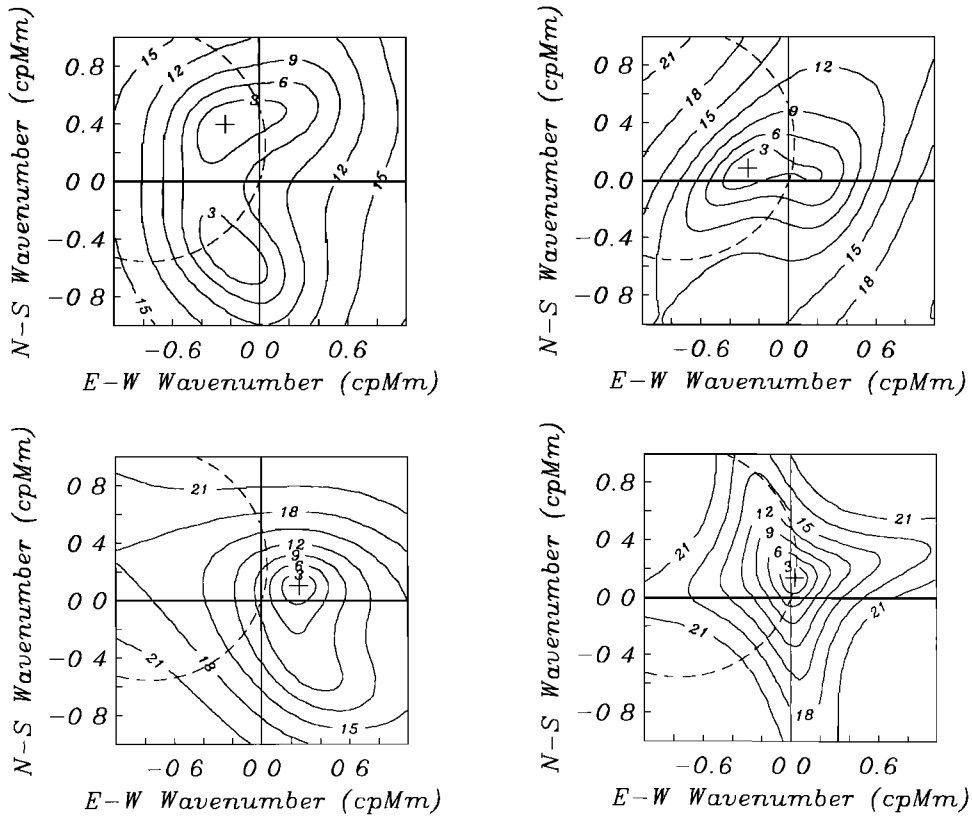

Fig. 30. Wavenumber spectra for curl at a period of 25 days for (clockwise from top left) grid points 2030, 2327, 2024, and 1727 located symmetrically to the west, north, east, and south of grid point 2027 shown in Figure 29. The spectral peak is denoted by a cross, and the contours are in decibels down from the peak. The spectra have 6 to 14 degrees of freedom, yielding a standard error of 3.4 to 5.5 dB. The peak power is, respectively, 4.40, 2.06, 1.85, and 2.63 $\times 10^{-15}$ dyn^2 cm^{-6} cpd^{-1} at the four sites.

spectrum peaks near the slowness circle appropriate for a given frequency. This is essentially a resonant Rossby wave response over a limited part of wavenumber space. By contrast, the coherence is the squared cross-spectrum between the oceanic and atmospheric variable over all wavenumbers normalized by the ocean and atmospheric frequency autospectra. As a consequence, the coherence will be reduced by the destructive interference of different wavenumbers which primarily reflects the wavenumber bandwidth of curl.

In section 5, it was noted that persistent coherence patterns were observed at 38-25 and 13 days with a fixed northeast forcing point near grid points 2027 and 2026 (Figures 10-11 and 13-14). Figure 29 shows MLM wavenumber spectra for curl at grid point 2027 for periods of 25, 19, 15, and 13 days using the time-bandwidths in Table 3. The spectra were computed using five FNOC sites in the form of a cross centered at the grid point of interest. The spectrum at 38 days is similar to that at 25 days. There is a reasonable matchup of the curl power peak with the slowness circle at all periods, but the broader wavenumber bandwidth at 19 and 15 days would result in lower velocity-to-curl coherence. Furthermore, the total power is about 2 times larger at 25 and 13 days than at 19 and 15 days. This suggests that strong resonant excitation of Rossby waves with a small wavenumber bandwidth might occur from this location for 25 and 13 days, but is less likely at 19 and 15 days, as is observed. Figure 30 shows curl wavenumber spectra at 25 days period for four other points located symmetrically around 2027 and situated ≈1000 km distant. Note the substantial variability in curl wavenumber characteristics with location. With the exception of the easternmost point (2024), these sites do not display wavenumber characteristics which are particularly favorable for narrow bandwidth Rossby wave excitation. Furthermore, even if Rossby waves were generated at grid point 2024, the matchup of the forcing peak and the slowness circle indicates that they would propagate nearly westward and hence would have a weaker zonal velocity signature than those from grid point 2027. Note that the actual power is somewhat higher at all four of these sites than at 2027. Thus, the enhanced power and persistent coherence patterns seen in the 20-to50-day and 10-to-14-day bands may be due to spatial inhomogeneity of curl, although this fails to explain all of the intersite differences.

Figures 28-30 provide a partial explanation both for the existence of persistent forcing hotspots and for the substantial frequency-dependent fluctuations in forcing location that has been observed. Comparable variability is observed at other periods, although there is an increasing bias toward eastward phase propagation of the forcing below 10 days. However, because the diameter of the slowness circle decreases with period, a smaller region of wavenumber space nearer the origin contains allowable wavenumbers for Rossby wave excitation. This means that progressively smaller directional fluctuations for curl have an increasingly large effect as the period drops. Figure 31 illustrates this for four points in the eastern North Pacific at 7.4-days period. While the power is generally eastward at all save the Gulf of Alaska site, significant power is present in the left half of the wavenumber plane, but with different directions

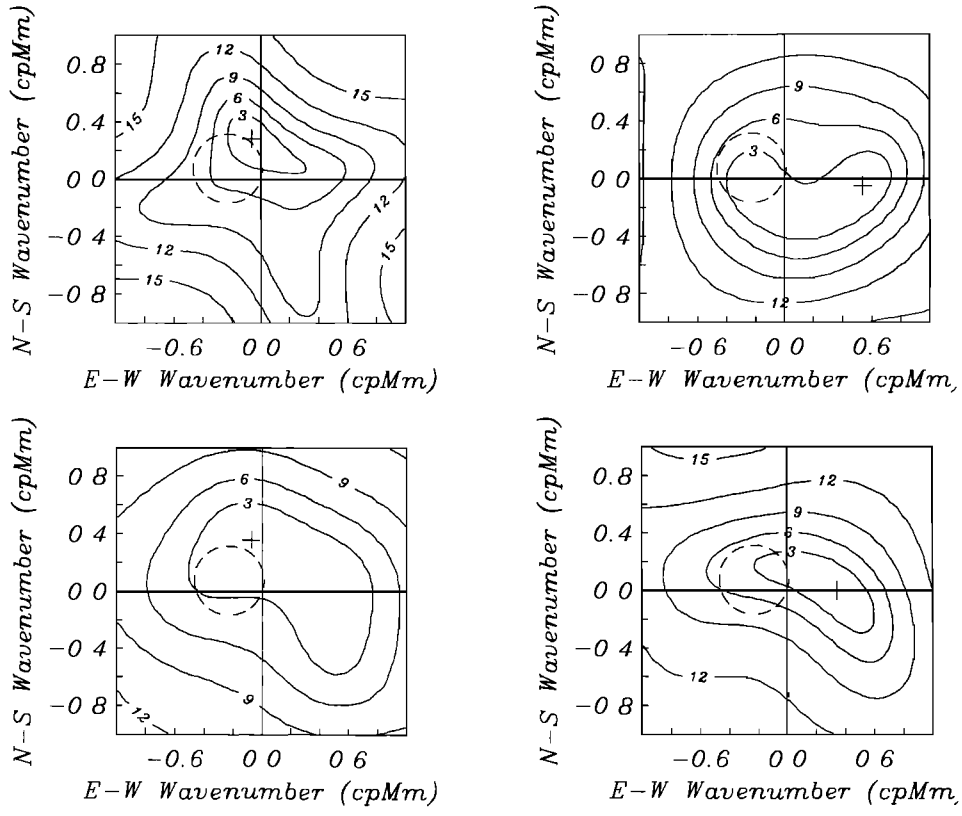

Fig. 31. Wavenumber spectra for curl at a period of 7.4 days for (clockwise from bottom left) grid points 2027, 2327, 2324, and 2024 located in the eastern North Pacific. The spectral peak is denoted by a cross, and the contours are in decibels down from the peak. The spectra have 12 to 22 degrees of freedom, yielding a standard error of 2.7 to 3.7 dB. The peak power is, respectively, 0.66, 1.53, 0.31, and 0.44 $\times 10^{-15}$ dyn^2 cm^{-6} cpd^{-1} at the four sites.

at each site, as denoted by the intersection of the 3 dB contour with the slowness circle. However, (9) for meridional velocity as shown in Figure 28 implies preferential selection of those wavenumbers lying near the zonal axis which may correspond to either eastward or westward group velocity. This may account in part for the larger azimuthal variability and multiplicity of the forcing that is observed at shorter periods for meridional velocity. At long periods, it is more unlikely that Rossby waves with large zonal wavenumber magnitudes will be observed, both because strong westward phase propagation of curl is rare and because (9) will filter them out. This helps explain the infrequent observation of western forcing regions at periods over 10 days.

While curl spatial nonstationarity will certainly explain much of the observed coherence pattern variability with period, it is unlikely to explain the intersite variability at a given period which is topographically induced. The influence of topography on the barotropic velocity observations has been suggested by the observations, but a quantitative understanding of its effects is currently lacking. A more complete picture must await the construction of suitable numerical simulations which incorporate real topography as well as real winds.

Acknowledgments. This paper is dedicated with respect to the memory of Henry M. Stommel, whose prodigious contributions to oceanography included a long-term interest in motional induction as an oceanographic tool. BEMPEX was supported at SIO by NSF grants OCE84-20578, OCE88-00783, and OCE89-22948.

REFERENCES

Brink, K.H., Evidence for wind-driven current fluctuations in the western North Atlantic, *J. Geophys. Res.*, *94*, 2029–2044, 1989.

Brown, W., W.H. Munk, F. Snodgrass, H. Mofjeld, and B. Zetler, MODE bottom experiment, *J. Phys. Oceanogr.*, *5*, 75–85, 1975.

Capon, J., High-resolution frequency-wavenumber spectrum analysis, *Proc. IEEE*, *57*, 1408–1418, 1969.

Capon, J., and N.R. Goodman, Probability distribution for estimators of the frequency-wavenumber distribution, *Proc. IEEE*, *58*, 1785–1786, 1970.

Chave, A.D., and D.S. Luther, Low-frequency, motionally induced electromagnetic fields in the ocean, 1. Theory, *J. Geophys. Res.*, *95*, 7185–7200, 1990.

Chave, A.D., J.H. Filloux, D.S. Luther, L.K. Law, and A. White, Observations of motional electromagnetic fields during EMSLAB, *J. Geophys. Res.*, *94*, 14,153–14,166, 1989.

Chave, A.D., D.S. Luther, and J.H. Filloux, Variability of the wind stress curl over the North Pacific: Implications for the oceanic response, *J. Geophys. Res.*, *96*, 18,361–18,379, 1991.

Cheney, R.E., J.G. Marsh, and B.D. Beckley, Global mesoscale variability from collinear tracks of Seasat altimeter data, *J. Geophys. Res.*, *88*, 4343–4354, 1983.

Cummins, P.F., The barotropic response of the subpolar North Pacific to stochastic wind forcing, *J. Geophys. Res.*, *96*, 8869–8880, 1991.

Cummins, P.F., and H.J. Freeland, Observation and modeling of wind-driven currents in the northeast Pacific, *J. Phys. Oceanogr.*, in press, 1992.

Dickson, R.R., W.J. Gould, P.A. Gurbutt, and P.P. Killworth, A seasonal signal in the ocean currents to abyssal depths, *Nature*, *295*, 193–198, 1982.

Filloux, J.H., Instrumentation and experimental methods for oceanic studies, in *Geomagnetism*, vol. 1, edited by J.A. Jacobs, pp. 143–248, Academic, San Diego, Calif., 1987.

Frankignoul, C., and P. Müller, Quasi-geostrophic response of an infinite β-plane ocean to stochastic forcing by the atmosphere, *J. Phys. Oceanogr.*, *9*, 104–127, 1979.

Koblinsky, C.J., The global distribution of f/H and the barotropic response of the ocean, *J. Geophys. Res.*, *95*, 3213–3218, 1990.

Koblinsky, C.J., and P.P. Niiler, The relationship between deep ocean currents and winds east of Barbados, *J. Phys. Oceanogr.*, *12*, 144–153, 1982.

Koblinsky, C.J., P.P. Niiler, and W.J. Schmitz, Observations of wind-forced deep ocean currents in the North Pacific, *J. Geophys. Res.*, *94*, 10,773–10,790, 1989.

Le Blond, P.H., and L.A. Mysak, *Waves in the Ocean*, 602 pp., Elsevier, New York, 1978.

Longuet-Higgins, M.S., Planetary waves on a rotating sphere, *Proc. R. Soc. London, Ser. A*, *279*, 446–473, 1964.

Luther, D.S., A.D. Chave, and J.H. Filloux, BEMPEX: A study of barotropic ocean currents and lithospheric electrical conductivity, *Eos Trans. AGU*, *68*, 618–619, 628–629, 1987.

Luther, D.S., A.D. Chave, J.H. Filloux, and P.F. Spain, Evidence for local and nonlocal barotropic responses to atmospheric forcing during BEMPEX, *Geophys. Res. Lett.*, *17*, 949–952, 1990.

Luther, D.S., J.H. Filloux, and A.D. Chave, Low-frequency, motionally induced electromagnetic fields in the ocean, 2, Electric field and Eulerian current comparison, *J. Geophys. Res.*, *96*, 12,797–12,814, 1991.

Müller, P., and C. Frankignoul, Direct atmospheric forcing of geostrophic eddies, *J. Phys. Oceanogr.*, *11*, 287–308, 1981.

Niiler, P.P., and C.J. Koblinsky, A local, time-dependent Sverdrup balance in the eastern North Pacific Ocean, *Science*, *229*, 754–756, 1985.

Philander, S.G.H., Forced oceanic waves, *Rev. Geophys.*, *16*, 15–46, 1978.

Rhines, P., Slow oscillations in an ocean of varying depth, Part 1. Abrupt topography, *J. Fluid Mech.*, *37*, 161–189, 1969.

Rhines, P., Edge-, bottom-, and Rossby waves in a rotating stratified fluid, *Geophys. Fluid Dyn.*, *1*, 273–302, 1970.

Samelson, R.M., Stochastically forced current fluctuations in vertical shear and over topography, *J. Geophys. Res.*, *94*, 8207–8215, 1989.

Samelson, R.M., Evidence for wind-driven current fluctuations in the eastern North Atlantic, *J. Geophys. Res.*, *95*, 11,359–11,368, 1990.

Samelson, R.M., Correction to "Evidence for wind-driven current fluctuations in the eastern North Atlantic" by R.M. Samelson, *J. Geophys. Res.*, *95*, 821–822, 1992.

Samelson, R.M., and B. Shrayer, Currents forced by stochastic winds with meridionally-varying amplitude, *J. Geophys. Res.*, *96*, 18,425–18,429, 1991.

Sanford, T.B., A.D. Chave, D.S. Luther, C.S. Cox, J.H. Filloux, and J.C. Larsen, Motional electromagnetic methods and WOCE, U.S. WOCE Tech. Rep. 3, 42 pp., U.S. WOCE Office, College Station, Tex., 1990.

Thomson, D.J., Spectrum estimation and harmonic analysis, *Proc. IEEE*, *70*, 1055–1096, 1982.

Thomson, D.J., and A.D. Chave, Jackknife error estimates for spectra, coherences, and transfer functions, in *Advances in Spectrum Analysis and Array Processing*, vol. 1, edited by S. Haykin, pp.58–113, Prentice-Hall, Englewood Cliffs, N.J., 1991.

Treguier, A.M., and B.L. Hua, Oceanic quasi-geostrophic turbulence forced by stochastic wind fluctuations, *J. Phys. Oceanogr.*, *17*, 397–411, 1987.

Willebrand, J.S., G.H. Philander, and R.C. Pacanowski, The oceanic response to large scale atmospheric disturbances, *J. Phys. Oceanogr.*, *10*, 411–429, 1980.

A.D. Chave, Woods Hole Oceanographic Institution, Woods Hole, MA 02543.

J.H. Filloux and D.S. Luther, Scripps Institution of Oceanography, Mail Code 0230, La Jolla, CA 92093.

(Received September 20, 1991;
revised March 5, 1992;
accepted March 5, 1992.)